Geoscience Frontiers 6 (2015) 875–893

HOSTED BY

Contents lists available at ScienceDirect

China University of Geosciences (Beijing)

Geoscience Frontiers

journal homepage: www.elsevier.com/locate/gsf

Research paper

Interpretation of residual gravity anomaly caused by simple shaped bodies using very fast simulated annealing global optimization

Arkoprovo Biswas*

Department of Earth and Environmental Sciences, Indian Institute of Science Education and Research (IISER) Bhopal, Indore By-pass Road, Bhauri, Bhopal 462 066, Madhya Pradesh, India

ARTICLE INFO

Article history:
Received 26 November 2014
Received in revised form
20 February 2015
Accepted 14 March 2015
Available online 2 April 2015

Keywords:
Gravity anomaly
Idealized body
Uncertainty
VFSA
Subsurface structure
Ore exploration

ABSTRACT

A very fast simulated annealing (VFSA) global optimization is used to interpret residual gravity anomaly. Since, VFSA optimization yields a large number of best-fitted models in a vast model space; the nature of uncertainty in the interpretation is also examined simultaneously in the present study. The results of VFSA optimization reveal that various parameters show a number of equivalent solutions when shape of the target body is not known and shape factor '*q*' is also optimized together with other model parameters. The study reveals that amplitude coefficient *k* is strongly dependent on shape factor. This shows that there is a multi-model type uncertainty between these two model parameters derived from the analysis of cross-plots. However, the appraised values of shape factor from various VFSA runs clearly indicate whether the subsurface structure is sphere, horizontal or vertical cylinder type structure. Accordingly, the exact shape factor (1.5 for sphere, 1.0 for horizontal cylinder and 0.5 for vertical cylinder) is fixed and optimization process is repeated. After fixing the shape factor, analysis of uncertainty and cross-plots shows a well-defined uni-model characteristic. The mean model computed after fixing the shape factor gives the utmost consistent results. Inversion of noise-free and noisy synthetic data as well as field data demonstrates the efficacy of the approach.

1. Introduction

One of the most imperative purposes in the interpretation of the gravity data is to determine the different types of subsurface structures and the position of the body. Numerous interpretative approaches have been developed in past and also significantly in the present time. Elucidation of the measured gravity anomaly by some idealized bodies such as cylinders and spheres remains an interest in exploration and engineering geophysics (e.g., Grant and West, 1965; Roy, 1966; Nettleton, 1976; Beck and Qureshi, 1989; Hinze, 1990; Lafehr and Nabighian, 2012; Hinze et al., 2013; Long and Kaufmann, 2013). The aim of gravity inversion is to estimate the parameters (depth, amplitude coefficient, location of the body and shape factor) of gravity anomalies produced by simple shaped structures from gravity observations.

Numerous interpretation methods have been developed to interpret gravity field data assuming fixed source geometrical models. In most cases, these methods consider the geometrical shape factor of the buried body being a priori assumed, and the depth variable may thereafter be obtained by different interpretation methods. These techniques include, for example, graphical methods (Nettleton, 1962, 1976), ratio methods (Bowin et al., 1986; Abdelrahman et al., 1989), Fourier transform (Odegard and Berg, 1965; Sharma and Geldart, 1968), Euler deconvolution (Thompson, 1982), neural network (Elawadi et al., 2001), Mellin transform (Mohan et al., 1986), least squares minimization approaches (Gupta, 1983; Lines and Treitel, 1984; Abdelrahman, 1990; Abdelrahman et al., 1991; Abdelrahman and El-Araby, 1993; Abdelrahman and Sharafeldin, 1995a), Werner deconvolution (Hartmann et al., 1971; Jain, 1976; Kilty, 1983), Walsh transformation (Shaw and Agarwal, 1990). Salem and Ravat (2003) presented a new automatic method for the interpretation of magnetic data, called AN-EUL which is a combination of the analytic signal and the Euler deconvolution method. Asfahani and Tlas (2012) developed the fair function minimization procedure. Fedi (2007) proposed a method called depth from extreme points

* Tel.: +91 755 6692442.
E-mail addresses: arkoprovo@gmail.com, abiswas@iiserb.ac.in.
Peer-review under responsibility of China University of Geosciences (Beijing).

http://dx.doi.org/10.1016/j.gsf.2015.03.001

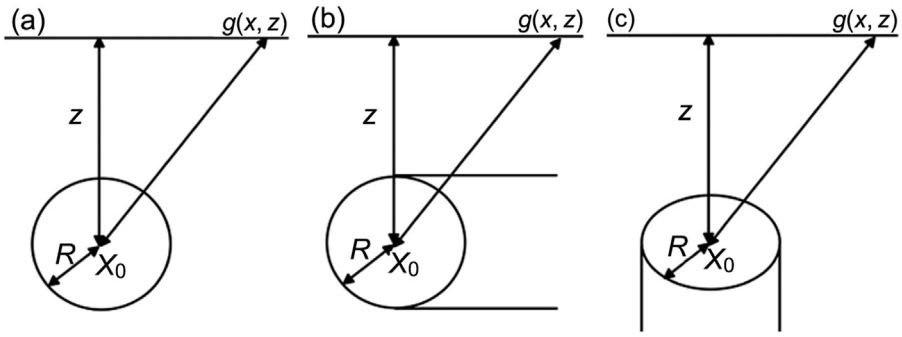

Figure 1. A diagram showing cross-sectional views, geometries and parameters of a sphere (a), an infinitely long horizontal cylinder (b) and a semi-infinite vertical cylinder (c).

(DEXP) to interpret any potential field. Continual least-squares methods (Abdelrahman and Sharafeldin, 1995b; Abdelrahman et al., 2001a, b; Essa, 2012, 2014) have been also developed. Regularized inversion method has also been developed by Mehanee (2014).

In general, the determination of the depth, shape factor, and amplitude coefficient of the buried structure is performed by some of these methods from the residual gravity anomaly. Moreover, location of the exact body is also an important parameter which also needs to be interpreted very precisely. Therefore, the precision of the results obtained by the above mentioned methods depends on the accuracy within which the residual anomaly can be separated from the observed gravity anomaly. Apart from versatile development in interpretation approaches, non-uniqueness of gravity data interpretation has not been addressed in most of the literature. Interpretation of gravity anomaly also suffers from this limitation. Several methods interpret only a few model parameters of the causative body (such as depth, shape factor, and amplitude coefficient). However, a precise interpretation of various parameters needs optimization of all model parameters together. This leads to much more ambiguous interpretation in comparison to finding a few parameters only. Some model parameters could be inter-dependent and estimating their actual values is equally important. Hence, in the present study, uncertainty associated with the interpretation of gravity data over simple shaped bodies (sphere and cylinder) is investigated using VFSA global optimization method. VFSA optimization is able to search a vast model space without compromising the resolution and it had been widely used in many geophysical applications (Sharma and Kaikkonen, 1999a,b; Sharma and Biswas, 2011, 2013; Sharma, 2012; Sen and Stoffa, 2013; Biswas and Sharma, 2015). VFSA's major advantage over other methods is that it has the ability to avoid becoming trapped in local minima. Another feature is that the partial derivatives (Frechet derivatives) and large scale matrix operations are avoided in such operations. Therefore, model parameters of simple bodies are optimized in a vast model space and ambiguities are analysed. Objective of the present study is to find a suitable interpretation steps that produces the utmost consistent model parameters and the slightest uncertainty for simple shaped bodies for gravity anomaly. Moreover, the objective is to invert and interpret the complete observed residual gravity data produced by some body fixed in the subsurface. In most of the cases, authors do not interpret all the model parameters which again lead to some erroneous results. In such case it is highly important to interpret and relevant that more the observed data and model parameter, the better is the inversion results and minimizes the uncertainty in the interpretation. The applicability of the proposed technique is assessed and discussed with the help of synthetic data and field examples taken from different parts of the world. The proposed method can be effectively used to interpret residual gravity anomaly data over simple bodies and can be successfully applied in deciphering subsurface structure and exploration in any area with least uncertainty in the final interpretation.

2. Formulation for forward gravity modelling

The general expression of a gravity anomaly $g(x)$ for a horizontal cylinder, a vertical cylinder, or a sphere-like structure at any point on the free surface along the principal profile in a Cartesian coordinate system (Fig. 1) is given by Gupta (1983), Abdelrahman et al. (2001a,b) and Essa (2007, 2014) as:

$$g(x) = k\left[\frac{z}{\left\{(x-x_0)^2+z^2\right\}^q}\right] \tag{1}$$

where, $q = 1.5$ (sphere), 1 (horizontal cylinder) and 0.5 (vertical cylinder) and $k = \frac{4}{3}\pi G\sigma R^3$ for $q = 1.5$; $k = 2\pi G\sigma R^2$ for $q = 1$ and $k = \frac{\pi G\sigma R^2}{z}$ for $q = 0.5$. k is the amplitude coefficient, z is the depth from the surface to the centre of the body (sphere or horizontal cylinder) or the depth from the surface to the top (vertical cylinder), q is the geometric shape factor, x_0 is the horizontal position coordinate, σ is the density contrast between the source and the host rock, G is the universal gravitational constant, and R is the radius of the buried structure.

3. Very fast simulated annealing global optimization method

3.1. Theoretical concept

Global optimization methods such as Simulated Annealing (SA), Genetic Algorithms (GA), Artificial Neural Networks (ANN) and Particle Swarm Optimization (PSO) have been applied in multi-parametric optimization of various geophysical data sets (Rothman, 1985, 1986; Dosso and Oldenburg, 1991; Sharma and Kaikkonen, 1998, 1999a,b; Juan et al., 2010; Sharma and Biswas, 2011, 2013; Sharma, 2012; Sen and Stoffa, 2013; Biswas and Sharma, 2014a,b, 2015). Simulated annealing is a focused random-search technique which exploits an analogy between the model parameters of an optimization problem and particles in an idealized physical system.

The conventional global optimization techniques (simulated annealing using a heat-bath algorithm or a genetic algorithm) compute the misfit for a large number of models in the model space. Subsequently they compute the probability of each model and try to concentrate in the region of high probability. In the present study, an advanced method of SA known as very fast simulated annealing (VFSA) is used, which does not compute misfit for a large number of models at a time but it moves in the model space randomly. It selects a new model, computes misfit and

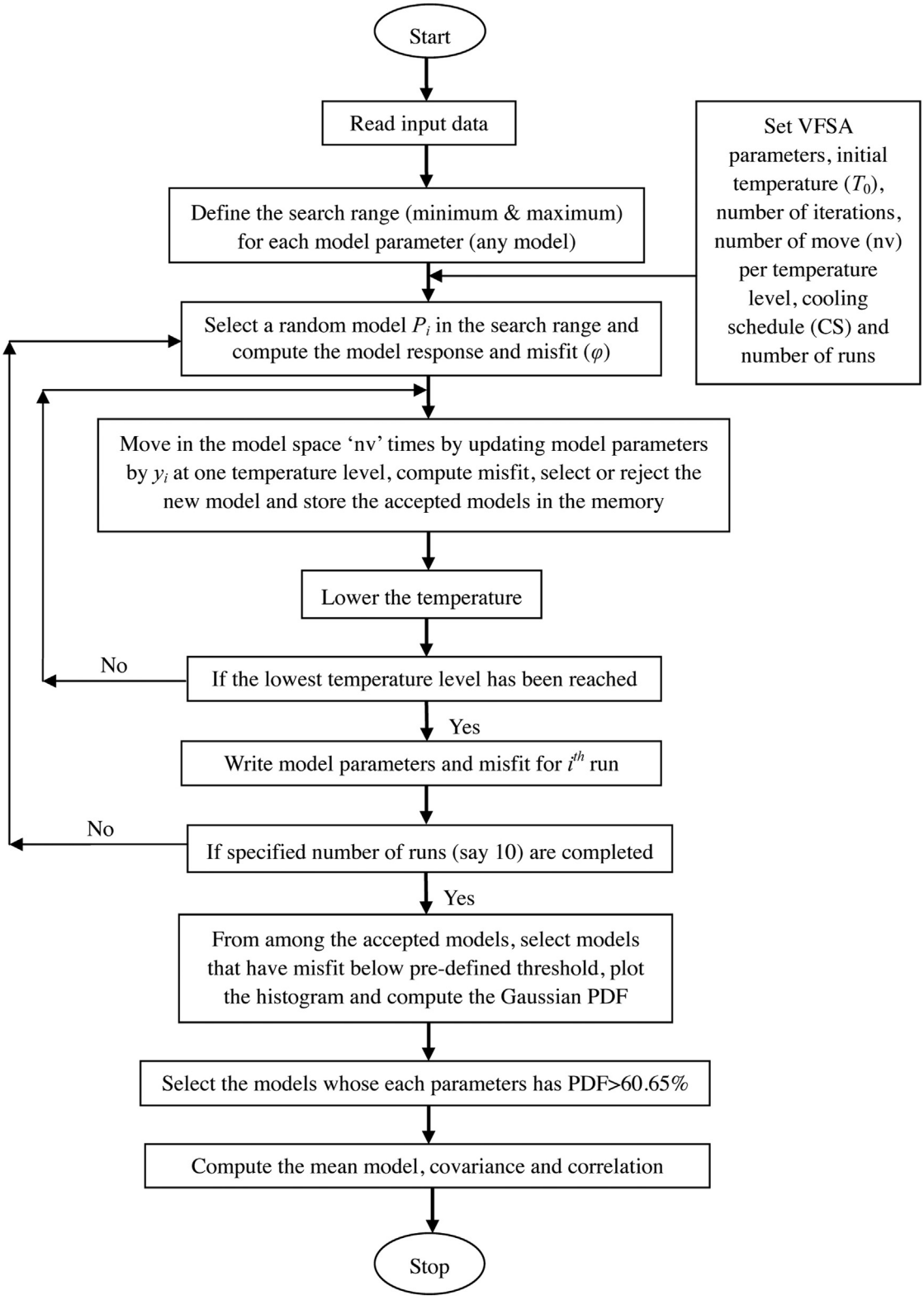

Figure 2. Flow chart of the whole VFSA process.

probability for this model, and then selects or rejects this model with respect to the previous model. Movement in the model space follows Cauchy probability distribution, which has a sharper peak than Gaussian distribution. This allows the temperature to be lowered at a faster rate in VFSA than conventional SA approach. Hence VFSA reaches the final temperature very rapidly (Sen and Stoffa, 2013). This technique has been widely used in many geophysical exploration and interpretation related to electrical and electromagnetic methods (Sharma and Kaikkonen, 1998, 1999a,b; Sharma and Verma, 2011; Sharma, 2012; Sharma and Biswas,

Table 1a
Actual model parameters, search range and interpreted mean model for noise free, 10% random noise with uncertainty for sphere (Model 1a).

Model parameters	Actual value	Search range	Mean model (noise-free)		Mean model (noisy data)	
			q variable	q fixed	q variable	q fixed
k (mGal × m^2)	5000	0–10000	5758.7 ± 617.7	4995.5 ± 14.9	5011.8 ± 919.7	5046.5 ± 40.9
x_0 (m)	250	100–500	250.0 ± 0.0	250.0 ± 0.0	245.5 ± 0.2	245.4 ± 0.2
z (m)	70	0–100	70.6 ± 0.7	70.0 ± 0.0	70.4 ± 0.7	70.4 ± 0.4
q	1.5	0–2	1.51 ± 0.0	1.5 (fixed)	1.51 ± 0.0	1.5 (fixed)
Misfit			2.4×10^{-5}	6.4×10^{-8}	4.4×10^{-4}	4.3×10^{-4}

2013). The VFSA optimization is also widely applied in non-geophysical problems and this shows efficacy of the VFSA optimization.

VFSA selects better models while moving randomly (guided/focused) in the multi-dimensional model space at the same and different temperature levels and finally yields a model with the lowest misfit. All good fitting models within the predefined misfit threshold are analysed to assess the global solution. Different approaches such as computation of mean model from the final solutions from different VFSA runs as well as other statistical approaches have been used to derive the global model. In a complex situation, if the VFSA process is repeated several times then a number of solutions with similar misfit can be obtained. Under such circumstances it is better to perform statistical analysis of various models showing a misfit lower than a predefined threshold value. Therefore in the present VFSA approach, all the accepted models are also stored in the memory for the posterior analysis.

Initially a model P_i (k, x_0, z, and q) is selected randomly in the model space $P_i^{min} \le P_i \le P_i^{max}$. The objective function (φ) between the observed and model response is calculated (Sharma and Biswas, 2013).

$$\varphi = \frac{1}{N}\sum_{i=1}^{N}\left(\frac{V_i^0 - V_i^c}{\left|V_i^0\right| + \left(V_{\max}^0 - V_{\min}^0\right)/2}\right)^2 \quad (2)$$

where N is number of data point, V_i^0 and V_i^c are the ith observed and model responses, $V_{\max}^0$ and $V_{\min}^0$ are the maximum and minimum values of the observed response respectively. Model parameters and the objective function of the above model are kept in memory and each parameter is updated. The updating factor y_i for the ith parameter is computed from the following equation (Sen and Stoffa, 2013):

$$y_i = \mathrm{sgn}(u_i - 0.5)T_i\left[\left(1 + \frac{1}{T_i}\right)^{|2u_i - 1|} - 1\right] \quad (3)$$

such that it varies between −1 and +1. In Eq. (3), u_i is a random number varying between 0 and 1, and T_i is the temperature. The updating factor y_i in Eq. (3) follows Cauchy probability distribution and hence all model parameters in their respective model space follow Cauchy probability distribution. Each parameter P_i is updated to P_i^{j+1} from its previous value P_i^j by the equation

$$P_i^{j+1} = P_i^j + y_i\left(P_i^{\max} - P_i^{\min}\right) \quad (4)$$

and thus a new model is obtained. Now the misfit corresponding to this new model is calculated and compared with the misfit of the earlier/previous model. If the misfit of this new model is less than the misfit for the earlier model, then the new model is selected with the probability exp(-$\Delta\varphi$/T) where $\Delta\varphi$ is the difference of the objective functions of both models. When the misfit of the new model is higher than that of the earlier model then a random number is drawn and compared with the probability. If the probability is greater than the random number drawn then also the new model is accepted with the same probability otherwise this model is rejected keeping the earlier model and its objective function in memory. Subsequently, the desired number of moves is made at the same temperature level by accepting and rejecting the new models according to above mentioned criterion and this concludes a single iteration. Movement in the model space at a particular one temperature level produces an improved model. After completing the preferred number of moves at the particular temperature, the temperature is lowered according to the following cooling schedule:

$$T_i(j) = T_{0i}\exp\left(-c_i j^{\frac{1}{M}}\right) \quad (5)$$

where j is the number of iterations (1, 2, 3 …), c_i is a constant which may vary for different model parameters and depends on the problem, T_{0i} is the initial temperature, which may also vary for different parameters and depends on the nature of the objective function considered for the optimization, and M is the number of model parameters. In the present study c_i is considered to be equal to 1 and the initial temperature has been taken as 1. Number of moves per temperature is chosen as 50 and 2000 iterations are performed to lower the temperature at a sufficiently low value. The parameter $1/M$ in Eq. (5) is replaced by 0.4 to get appropriate reduction of temperature to the lowest temperature level in a fixed number of iteration. Also at the lowest temperature level, misfit will be the lowest. It is interesting to note that $1/M$ is 0.25 for 4 parameters, 0.125 for 8 parameters and so on. With such a small value, a large number of iterations are required for convergence (Sharma and Kaikkonen, 1998). Therefore, in order to reduce the number of iteration to reach the required lowest temperature level value of $1/M$ parameter is adjusted. The value of $1/M = 0.4$ has been set based on experience from various VFSA studies (Sharma and Kaikkonen, 1998, 1999a; Sharma and Biswas, 2013; Biswas and Sharma, 2014a,b).

After reducing the temperature to a lower level, once again the desired number of moves is made and the selection/rejection criterion discussed above is followed. Subsequently, the temperature is reduced gradually using Eq. (5) to a sufficiently low value, selecting better and better models at each temperature level. After completing the predefined iterations (say 2000), one solution is obtained. The whole procedure is repeated several times to obtain a number of solutions and each time the process starts from a randomly selected model in the predefined model space. The model parameters obtained in different runs could be the same for a well posed simple problem. However, they could be different according to the physics of the problem for complex problems.

3.2. Global model and uncertainty analysis

A single run of global converging algorithms is not sufficient to find the global solution (Sen and Stoffa, 2013). Hence, a number of good fitting models are optimized (10 VFSA runs in the present study). Model parameters (k, x_0, z, and q) of these good fitting models may disagree from each other and lie in a wide range in the

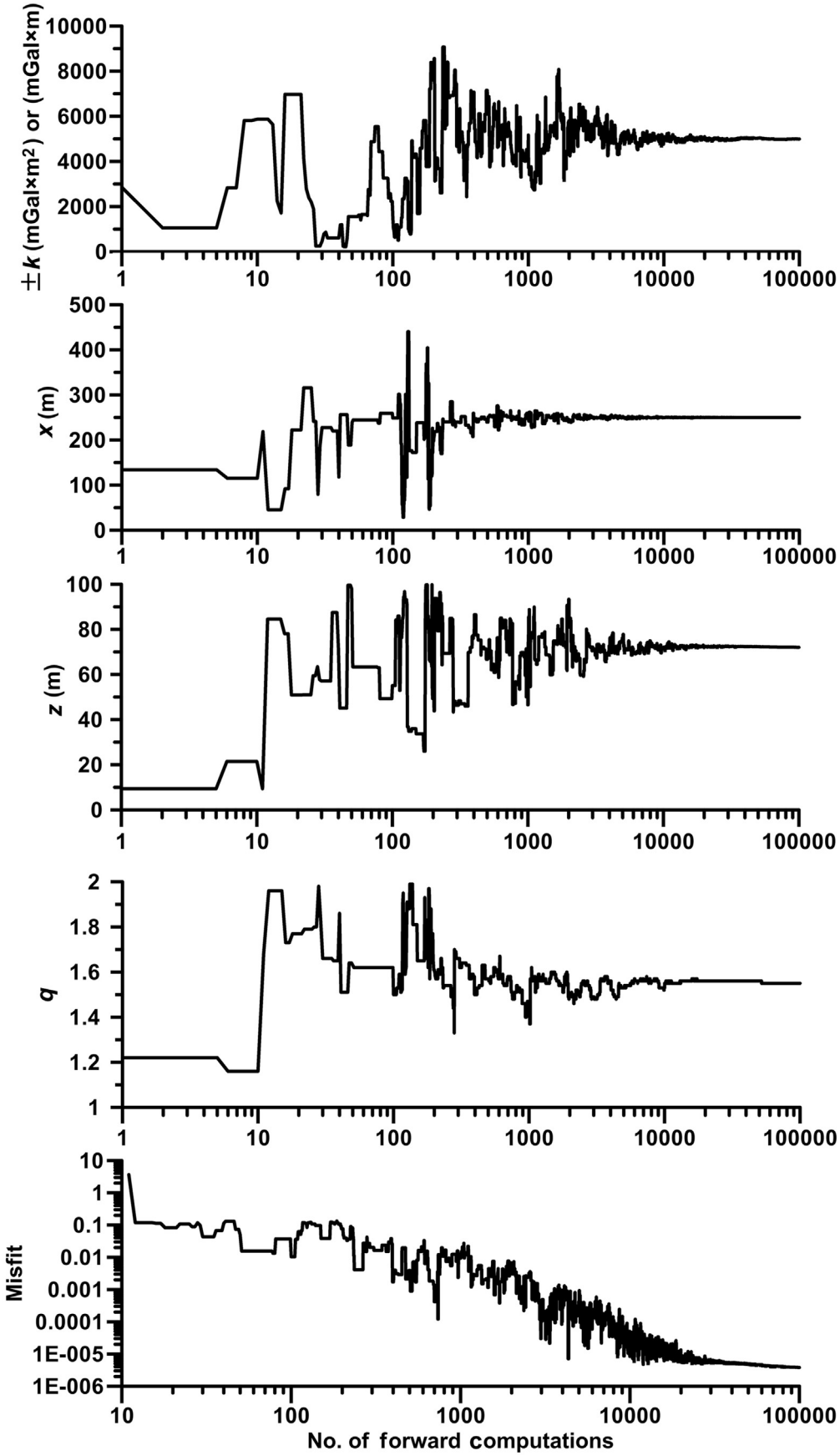

Figure 3. Convergence pattern for various model parameters and misfit.

multi-dimensional model space. It is necessary to sample the models from the most suitable region (where a large number of models are located) of the model space. Different sampling techniques have been used by different scientists (Mosegaard and Tarantola, 1995; Sen and Stoffa, 1996) to obtain the global model and minimize uncertainty in the solution. Sampling in the model space is based on different statistical distributions and could differ from one geophysical data to other.

To acquire a best fitting model, computations are performed at 2000 different temperature levels with 50 numbers of moves (nv) at one temperature level. The VFSA procedure is repeated 10 times and the 10 best fitting solutions are obtained. Thus 10^6 models and their misfit are stored in memory where misfit varies from a large value to a very small value. Out of these models, repeated models as well as models whose misfit is higher than the defined threshold (0.0001 for noise-free synthetic data and 0.01/0.02 for noisy and field data) value are discarded. Therefore, only models that fit the observed response up to certain degree are selected for statistical analysis. First, a histogram is prepared of all models that have misfit smaller than the predefined threshold value. Subsequently, posterior probability distribution is computed for all better-fitting models. Subsequently, Gaussian Probability Density Function (PDF) is computed. The Gaussian probability density function f_y (y, μ, σ^2) of a variable y (k, x_0, z, and q) is given by

$$f\left(y,\mu,\sigma^2\right) = \frac{1}{\sigma\sqrt{2\pi}} e^{-\frac{1}{2}\left(\frac{y-\mu}{\sigma}\right)^2} \quad (6)$$

Table 1b
Correlation matrix for sphere (Model 1a with q variable).

	k (mGal × m^2)	x_0 (m)	z (m)	q
k (mGal × m^2)	1.000	−0.013	0.981	0.998
x_0 (m)	−0.013	1.000	−0.001	−0.015
z (m)	0.981	−0.001	1.000	0.980
q	0.998	−0.015	0.980	1.000

In a Gaussian distribution, parameters denoted as μ and σ are the mean and standard deviation, respectively, of the variable y. In the present study, global model and associated uncertainty are obtained using the following approach. After computing the PDF for all selected models using Eq. (6), the maximum PDF for each model parameter is determined. Subsequently, for selection of good models with high PDF for the computation of the mean model, a 60.65% (one standard deviation) limit for the PDF is set for each parameter. In a Gaussian probability density distribution, probability density is 60.65% of its peak value at one standard deviation from the mean. If any parameter (k, x_0, z, and q) of a model has PDF lower than one standard deviation then that model is located in the undesired region of the model space and discarded. This results in sampling of the most appropriate region of the model space of the high probability region in multidimensional model space. Finally, only those models in which all model parameters have a PDF greater than one standard deviation are selected for computation of the mean model and uncertainty. It is observed that such a mean model is very close to the global model and the global model is

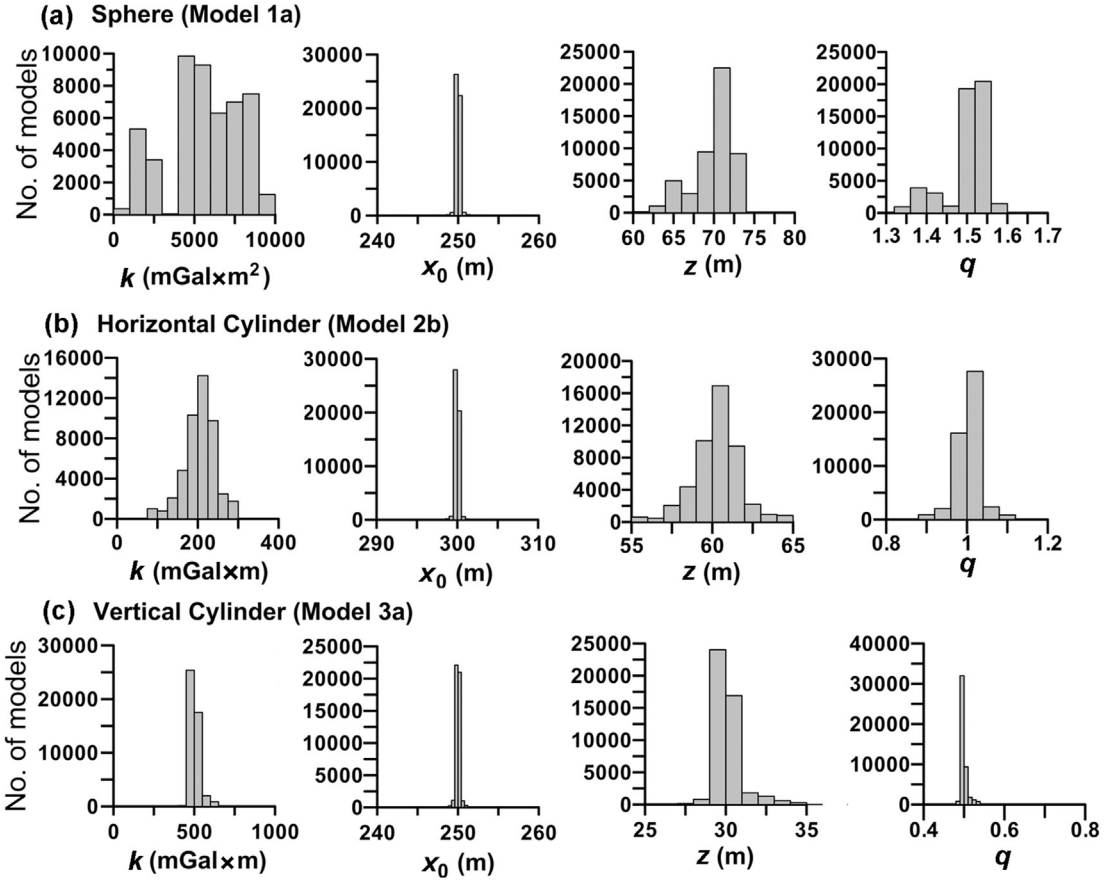

Figure 4. Histograms of all accepted models having misfit $<10^{-4}$ for noise-free synthetic data and PDF (q free) (a) sphere-Model 1a, (b) horizontal cylinder-Model 2b and (c) vertical cylinder-Model 3a.

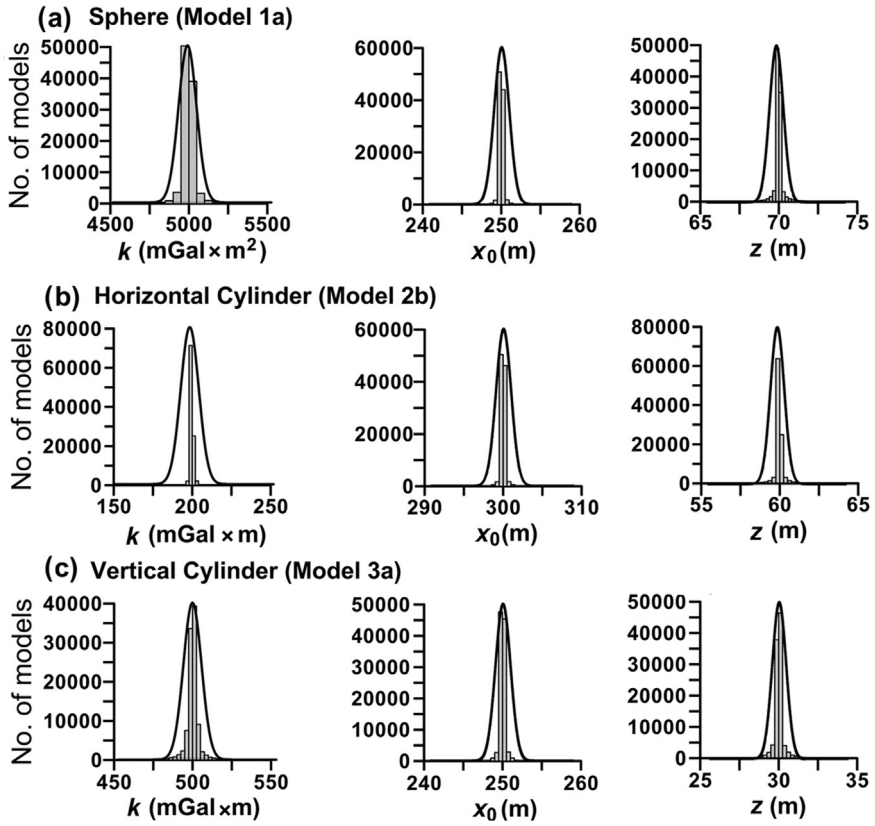

Figure 5. Histograms of all accepted models having misfit $<10^{-4}$ for noise-free synthetic data and PDF (q fixed) (a) sphere-Model 1a, (b) horizontal cylinder-Model 2b and (c) vertical cylinder-Model 3a.

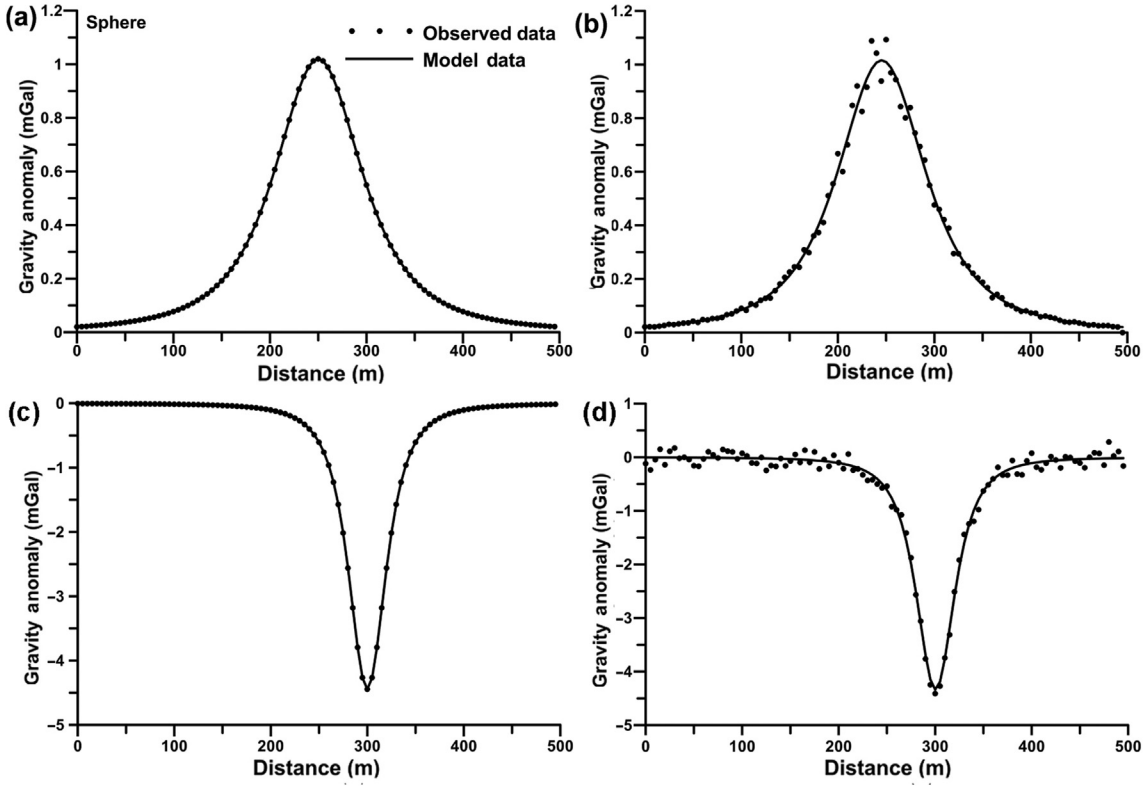

Figure 6. Fittings between the observed and model data for sphere: Model 1a–(a) noise-free synthetic data and (b) noisy synthetic data, Model 1b–(c) noise-free synthetic data and (d) noisy synthetic data.

Table 1c
Correlation matrix for sphere (Model 1a with q fixed).

	k (mGal × m^2)	x_0 (m)	z (m)
k (mGal × m^2)	1.000	−0.034	0.891
x_0 (m)	−0.034	1.000	−0.022
z (m)	0.891	−0.022	1.000

always located within the uncertainty estimated in the mean model. The mean model is computed from the new best models (NM) where each model parameter has a PDF larger than the defined threshold value (one standard deviation) using the expression

$$\overline{P_i} = \frac{1}{NM}\sum_{n=1}^{NM} P_n \tag{7}$$

In the above equation, NM is the number of models satisfying the above-noted criterion of a higher PDF. Subsequently, the covariance and correlation matrices are computed using the equations (Tarantola, 2005)

$$CovP(i,j) = \frac{1}{NM}\sum_{n=1}^{NM}\left(P_{i,n} - \overline{P_i}\right)\left(P_{j,n} - \overline{P_j}\right) \tag{8}$$

$$\text{and } CorP(i,j) = \frac{CovP(i,j)}{\sqrt{CovP(i,i) \times CovP(j,j)}} \tag{9}$$

In Eqs. (8) and (9) i and j vary from 1 to number of model parameters. The correlation matrix formed with these solutions fitting well to the observed response conveys the relationship of the parameters and associated physics. The square roots of the diagonal elements of the covariance matrix represent the uncertainties in the mean model parameters.

The code was developed in Window 7 environment using MS FORTRAN Developer studio on a simple desktop PC with Intel Pentium Processor. For each step of optimization, a total of 10^6 forward computations (2000 iterations × 50 number of moves × 10 VFSA runs) were performed and accepted models stored in memory. Next, models with misfit smaller than the predefined threshold are selected and the statistical mean model and the associated uncertainty are also computed. A flow chart for the whole VFSA process is given in Fig. 2.

4. Results

4.1. Theoretical example

The VFSA global optimization is implemented using noise-free and noisy synthetic data (10% uniformly random noise i.e., multiplied by a random draw between 1 and 1.10 and 20% Gaussian noise i.e., multiplied by a Gaussian random value with mean 1 and standard deviation 0.2) for a sphere, horizontal and vertical cylinder-type model. Initially, all model parameters are optimized for each data set. Consequently, the shape factor is fixed to the nearest structural feature, 1.5 for sphere, 1.0 for horizontal cylinder and 0.5 for vertical cylinder, and optimization procedure is repeated. To highpoint the strength of the method in finding the accurate model parameters, search ranges for various model parameters are kept wide and same in both steps. However, in principle, when the shape factor is fixed in the second step, one can reduce the search range for each model parameter on the basis of results depicted after the first step.

It is emphasized that in nature actual structures may not have the standard geometrical shape such as sphere, horizontal cylinder, vertical cylinder or sheet-type structures. Therefore, modelling and inversion of actual field data using above mentioned standard geometrical formulation may not yield the actual subsurface structure. Any, deviation of the actual structure from the modelled structure (sphere, cylinder, etc.) can be understood as orderly eccentricities from the modelled curves caused by the difference from three standard geometrical structures. Under such circumstances, the multi-dimensional objective (misfit) function will be extremely complex and simple inversion approach may fail to illustrate the subsurface structure. Hence, global optimization is even more necessary to deal with such condition. Moreover, it should be highlighted that irregular shaped bodies cannot be determined very precisely using any interpretation method unless and until multiple bore-holes drilled data are available. The main purpose is to find out the near probable shape, depth at where the body is located and the exact location of the body from the surface, which can be effectively used for drilling purpose.

4.1.1. Sphere (noise free and 10% random noisy – Model 1a)

At first, synthetic data (negative anomaly) are generated using Eq. (1) for a spherical model (Table 1a) and 10% random noise is added to the synthetic data. Inversion is performed using noise-free and noisy synthetic data to retrieve the actual model parameters and study the effect of noise on the interpreted model parameters. Initially, a suitable search range for each model parameter is selected and a single VFSA optimization is executed. After studying the proper convergence of each model parameter (k, x_0, z, and q) and misfit (Fig. 3) by adjusting VFSA parameters (such as initial temperature, cooling schedule, number of moved per temperature and number of iterations), 10 VFSA runs are performed. Subsequently, histograms (Fig. 4a) are prepared using accepted models whose misfit is lower than10^{-4}. The histograms in Fig. 4a depict that 3 model parameters (k, z, and q) show a wide ranging solutions. For example, k varies from 0–10,000 mGal × m^2 with its peak around 5000 mGal × m^2. Similarly, z, and q also vary over a wide range with histogram peaks at different values than their actual values for each model parameter. A statistical mean model is computed using models that have misfit lower than 10^{-4} and lie within one standard deviation. Table 1a depicts that the estimated mean model is far from the actual model and also it shows a large uncertainty (e.g. k). Other parameters x_0, z, and q of the mean model are quite close to their actual values but actual model is not located within the estimated uncertainty. Table 1b shows correlation matrix computed from the best fitted models lying within one standard deviation. It reveals a strong correlation between various model parameters.

Table 1d
Actual model parameters, search range and interpreted mean model for noise free, 20% Gaussian noise with uncertainty for sphere (Model 1b).

Model parameters	Actual value	Search range	Mean model (noise-free)		Mean model (noisy data)	
			q variable	q fixed	q variable	q fixed
k (mGal × m^2)	−4000	−8000–0	−4728.6 ± 557.5	−4000.5 ± 13.9	−2242.3 ± 657.4	−4075.9 ± 62.7
x_0 (m)	300	100–500	300.0 ± 0.0	300.0 ± 0.0	300.3 ± 0.1	300.3 ± 0.2
z (m)	30	0–60	30.4 ± 0.3	30.0 ± 0.0	29.4 ± 0.7	30.6 ± 0.4
q	1.5	0–2	1.52 ± 0.0	1.5 (fixed)	1.43 ± 0.0	1.5 (fixed)
Misfit			2.6×10^{-6}	1.3×10^{-8}	1.9×10^{-3}	1.8×10^{-3}

Table 2a
Actual model parameters, search range and interpreted mean model for noise free, 10% random noise with uncertainty for horizontal cylinder (Model 2a).

Model parameters	Actual value	Search range	Mean model (noise-free)		Mean model (noisy data)	
			q variable	q fixed	q variable	q fixed
k (mGal × m)	−500	−1000–0	−521.4 ± 25.7	499.8 ± 1.0	−424.5 ± 37.4	−491.3 ± 3.7
x_0 (m)	250	100–500	250 ± 0.0	250.0 ± 0.0	244.7 ± 0.2	244.6 ± 0.2
z (m)	20	0–50	20.2 ± 0.2	20.0 ± 0.0	19.5 ± 0.3	20.0 ± 0.3
q	1.0	0–2	1.01 ± 0.0	1.0 (fixed)	0.98 ± 0.0	1.0 (fixed)
Misfit			2.2×10^{-7}	8.3×10^{-9}	1.2×10^{-3}	1.2×10^{-4}

This indicates that model parameters are inter-dependent and cannot be determined uniquely. Therefore, such a solution is not reliable and cannot be used for the interpretation.

To avoid above untrustworthy result, subsequent steps are applied to get the mean model close to the actual model. It has been observed from the histogram in Fig. 4a that q varies from 1.3 to 1.65; this means optimization algorithm indicates a spherical structure with its peak near to 1.5. Hence q is fixed at 1.5 and VFSA optimization is repeated. Fig. 5a depicts the histogram of all accepted models with misfit less than 10^{-4}. Fig. 5a also reveals that model distribution follows the Gaussian distribution. Therefore, the Gaussian PDF of all models with misfit lower than 10^{-4} are computed and overlaid on the histogram in Fig. 5a. Finally, models whose each parameter lie within one standard deviation of the PDF are selected to compute the statistical mean model and associated uncertainty (Table 1a). Fig. 6a depicts a comparison between the observed and the mean model response. Table 1a depicts the interpreted mean model and associated uncertainty. Table 1c presents the correlation matrix computed from models lying within one standard deviation when q is fixed. The correlation matrix shows that k is positively correlated with depth (z) and negatively correlated with location (x_0). This means that if k increases z should increase and x_0 must decrease. These correlations are in accordance with the physics of the problem.

Next, VFSA optimization is performed using 10% random noise added data for Model 1a (Table 1a). The convergence of each model parameter and reduction of misfit is studied for a single solution. After observing the reduction of misfit systematically and stabilization of each model parameter during later iteration, ten VFSA runs are performed. It is important to mention that during the first step, ten VFSA runs are performed by optimizing all model parameters. A statistical mean model is computed and presented in Table 1a. Like noise-free data, here also again a large uncertainty in k has been observed. The results have been depreciated in the presence of noise in comparison to the inversion of noise-free data. The value of q is obtained as 1.51 and that produces an uncertain estimate for amplitude coefficient and misfit gets higher. As it can be seen that q is optimized between 0–2 but it is estimated as 1.51 which indicates a spherical body.

Subsequently, q is fixed at 1.5 like noise-free data and 10 VFSA runs are performed again. Misfits of accepted models vary from $1–10^{-3}$ to 10^{-4} (10% random noisy data) with iteration. Now, models that have misfit less than 0.01 are selected for statistical analysis. For brevity the histogram for noisy data is not presented here

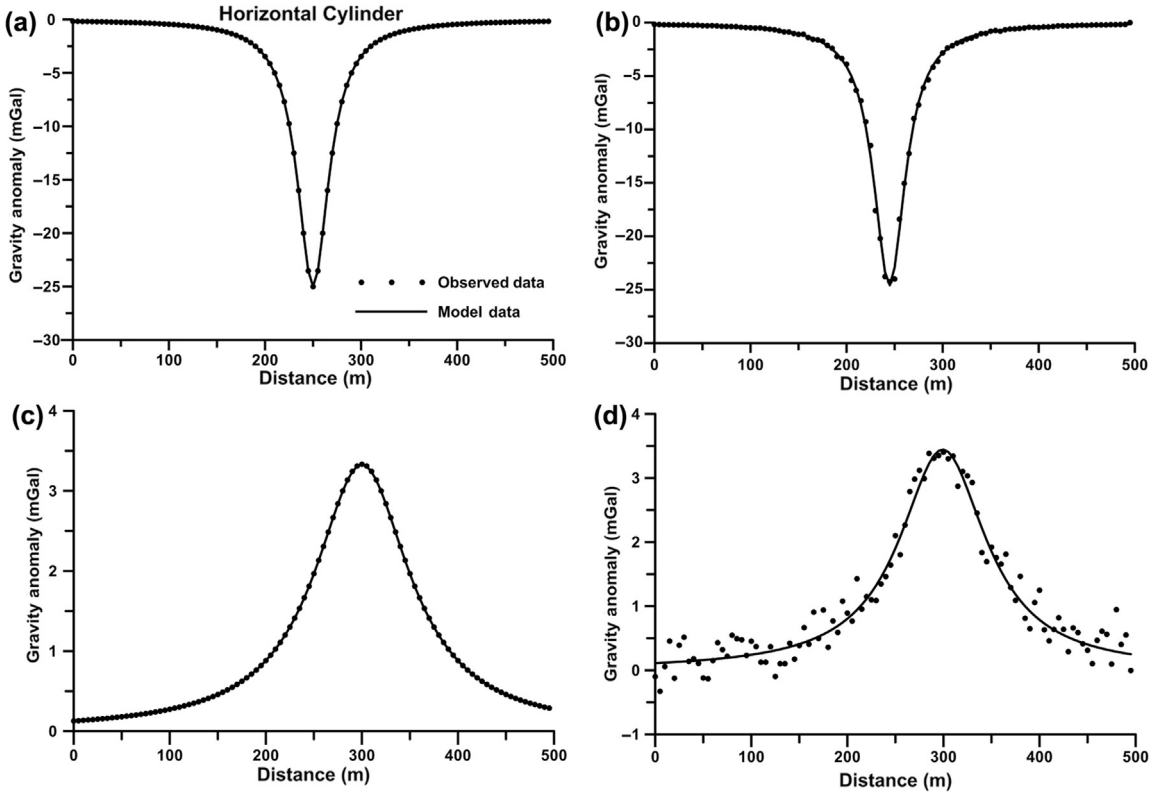

Figure 7. Fittings between the observed and model data for horizontal cylinder: Model 2a–(a) noise-free synthetic data and (b) noisy synthetic data, Model 2b–(c) noise-free synthetic data and (d) noisy synthetic data.

Table 2b
Actual model parameters, search range and interpreted mean model for noise free, 20% Gaussian noise with uncertainty for horizontal cylinder (Model 2b).

Model parameters	Actual value	Search range	Mean model (noise-free)		Mean model (noisy data)	
			q variable	q fixed	q variable	q fixed
k (mGal × m)	200	0–500	210.3 ± 22.6	199.6 ± 0.5	227.4 ± 27.7	188.9 ± 0.8
x_0 (m)	300	100–500	300 ± 0.0	300.0 ± 0.0	299.4 ± 0.2	299.3 ± 0.2
z (m)	60	0–100	60.3 ± 0.8	59.9 ± 0.0	55.9 ± 0.8	54.8 ± 0.3
q	1.0	0–2	1.01 ± 0.0	1.0 (fixed)	1.02 ± 0.0	1.0 (fixed)
Misfit			5.0×10^{-6}	3.3×10^{-7}	7.7×10^{-3}	7.6×10^{-4}

which is similar to Fig. 4a. The mean model presented in Table 1a for noisy data shows that actual model lie outside the appraised uncertainty. It is important to highlight that once any kind of noise added on the synthetic data then actual model is not known precisely. In such situation estimated uncertainty shows the accuracy of the solution. It can be seen for noise-free synthetic data, the actual model is located within the estimated uncertainty. The nature of uncertainty remains the same as observed for noise-free data. Fig. 6b depicts a comparison between the observed and the mean model data for noisy-synthetic data.

4.1.2. Sphere (noise free and 20% Gaussian noisy – Model 1b)

In this model (Model 1b), synthetic gravity anomaly (positive) is again generated to test whether the method can actually determine both negative and positive gravity anomalies. Like Model 1a, VFSA optimization is again performed. Next, 20% Gaussian noise is added to the data to test whether it can actually retrieve the actual model parameters. For brevity, histogram is not given and is same like Model 1a. The interpreted mean model parameters are given in Table 1d. Fig. 6c and d shows the fittings between the observed and mean model for synthetic noise free and 20% Gaussian noisy data. Again the nature of uncertainty remains the same as observed for noise-free data and noisy data as in case of Model 1a.

4.1.3. Horizontal cylinder (noise free and 10% random noisy – Model 2a)

First, forward response (negative anomaly) is generated for Model 2a (Table 2a) and again 10% random noise is added to the response. Optimization is performed for both noise-free and noisy synthetic data in similar way as it was done for a Model 1a (sphere). The histogram of accepted model with misfit lower than 10^{-4} after 10 VFSA runs clearly shows that q points towards 1.01 depicting a horizontal cylindrical type structure (Fig. 4b, like Model 2b). As usual when q is also kept variable then the mean model has a large uncertainty and actual model locate outside of the estimated uncertainty in the mean model, which is incorrect. Subsequently, q is fixed at 1.0 and 10 VFSA runs are performed. Fig. 5b shows the histogram and PDF of models with misfit lower than 10^{-4} (like Model 2b). The mean model is computed using the models in high PDF region of the model space and presented in Table 2a. The actual model is located within the estimated uncertainty in the mean model. Fig. 7a depicts a comparison between the observed and mean model response. The correlation matrix reveals a similar nature to that depicted in Table 1b and c for Model 1a.

VFSA optimization is carried out for 10% random noise added synthetic data for this model also and mean model is computed accordingly. Table 2a presents the interpreted mean model parameters and uncertainty when q is kept variable between 0–2 as well as fixed at 1.0. Here again it has been observed that the actual model is located outside the estimated uncertainty in the mean model for the reason as discussed for Model 1a. Fig. 7b depicts a comparison between the observed and mean model response.

4.1.4. Horizontal cylinder (noise free and 20% Gaussian noisy – Model 2b)

In this model (Model 2b), synthetic gravity anomaly (positive) is again generated to test whether the method can actually determine both negative and positive gravity anomalies. Like Model 2a, VFSA optimization is again performed the same way as it is done for Model 2a. The histogram of accepted model with misfit lower than 10^{-4} after 10 VFSA runs clearly shows that q points towards 1.01 depicting a horizontal cylindrical type structure (Fig. 4b). Fig. 5b shows the histogram and PDF of models with misfit lower than 10^{-4}. Next, 20% Gaussian noise is added to the data to test whether it can actually retrieve the actual model parameters. The interpreted mean model parameters are given in Table 2b. Fig. 7c and d shows the fittings between the observed and mean model for synthetic noise free and 20% Gaussian noisy data.

4.1.5. Vertical cylinder (noise free and 10% random noisy – Model 3a)

The corresponding theoretical noise-free and noisy data (positive anomaly) inversion is also carried out for Model 3a that represents a vertical cylinder (Table 3a). Fig. 4c shows the histogram when all model parameters are optimized during 10 VFSA runs. Fig. 4c also reveals that various good fittings models are located in a wide range like Fig. 4a and b when q is also optimized. It is obvious from Fig. 4c and Table 3a that q clearly indicates towards 0.51 even though its search range was 0–2. Subsequently, q is fixed at 0.5 and VFSA optimization is performed. Now the histogram (Fig. 5c) of good fitting models is centred on the actual model parameters. Gaussian PDF is computed using good fitting models and superimposed on the histogram. The mean model and uncertainty is computed from models lying with one standard deviation (in high PDF region) and shown in Table 3a. The actual value of k is located within the estimated uncertainty. Uncertainties in other model parameters are almost insignificant. Fig. 8a shows the fittings between the observed and mean model response.

Table 3a
Actual model parameters, search range and interpreted mean model for noise free, 10% random noise with uncertainty for vertical cylinder (Model 3a).

Model parameters	Actual value	Search range	Mean model (noise-free)		Mean model (noisy data)	
			q variable	q fixed	q variable	q fixed
k (mGal × m)	500	0–1000	499.5 ± 5.5	500.0 ± 1.2	557.1 ± 18.5	495.3 ± 5.7
x_0 (m)	250	100–500	250.0 ± 0.0	250.0 ± 0.0	250.2 ± 0.5	250.1 ± 0.5
z (m)	30	0–60	29.9 ± 0.2	30.0 ± 0.0	32.3 ± 0.6	30.4 ± 0.5
q	0.5	0–2	0.51 ± 0.0	0.50 (fixed)	0.52 ± 0.0	0.50 (fixed)
Misfit			1.1×10^{-7}	9.2×10^{-9}	6.9×10^{-4}	6.7×10^{-4}

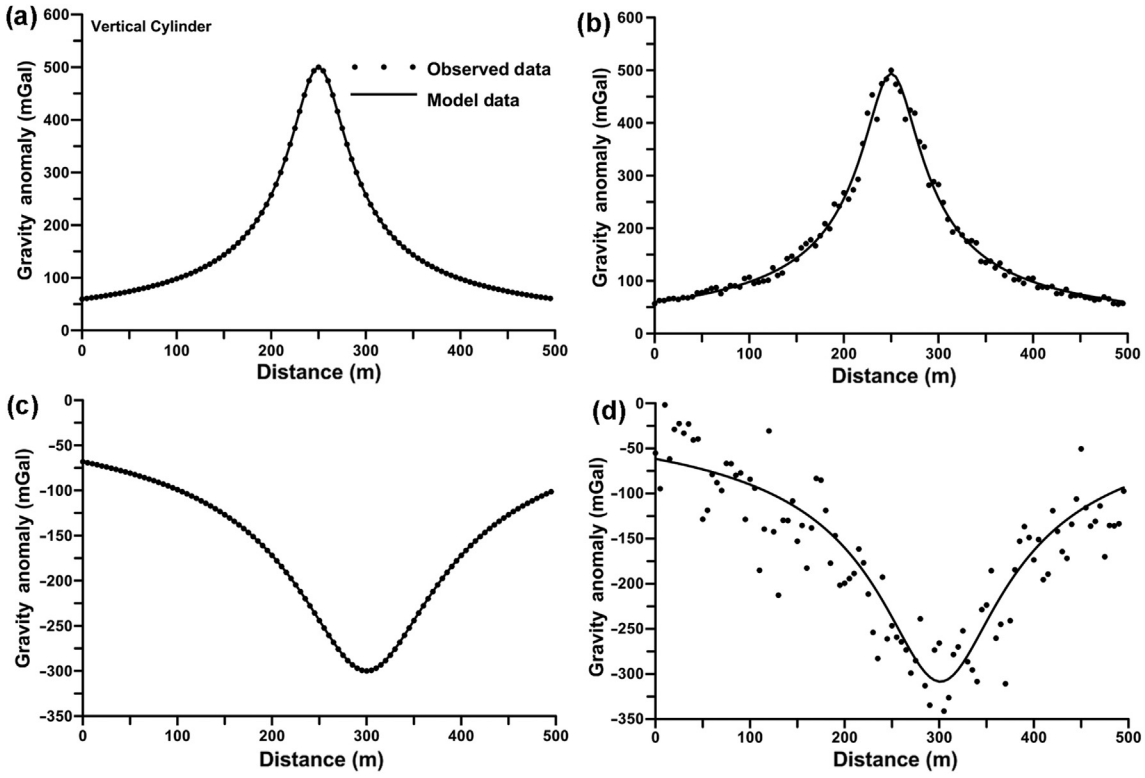

Figure 8. Fittings between the observed and model data for vertical cylinder: Model 3a–(a) noise-free synthetic data and (b) noisy synthetic data, Model 3b–(c) noise-free synthetic data and (d) noisy synthetic data.

Next, noisy-synthetic data for vertical cylinder is inverted to optimize its model parameter. After finding q pointing towards 0.52 for noisy data also, it was fixed at 0.5 and 10 VFSA runs are performed. Once again, models that have misfit less than 0.01 are selected for statistical analysis. The mean model is computed from models lying in one standard deviation and presented in Table 3a. Fig. 8c depicts a comparison between the observed and mean model response. Table 3a depicts the interpreted mean model and associated uncertainty when q is variable and fixed.

4.1.6. Vertical cylinder (noise free and 20% Gaussian noisy – Model 3b)

In Model 3b, synthetic gravity anomaly (negative) is again generated to test whether the method can truly define both negative and positive gravity anomalies for vertical cylindrical structure. Like Model 3a, VFSA optimization is again repeated the same way as it is done for Model 3a. The histogram of accepted model with misfit lower than 10^{-4} after 10 VFSA runs clearly shows that q points towards 0.51 depicting a vertical cylindrical type structure (like Fig. 4c). Like Fig. 5c, it also shows the histogram and PDF of models with misfit lower than 10^{-4}. Next, 20% Gaussian noise is added to the data to test whether it can actually retrieve the actual model parameters. The interpreted mean model parameters are given in Table 3b. Fig. 8c and d shows the fittings between the observed and mean model for synthetic noise free and 20% Gaussian noisy data.

4.2. Cross plot analysis

4.2.1. Sphere (noise free and 10% random noisy – Model 1a)

Fig. 9a depicts cross-plots between the model parameters k, z, and q using accepted models with misfit lower than 10^{-4} (grey) and models within the pre-defined high PDF region (black) when q is free. This shows that for a particular z and q, k shows a wide range of solutions when q is free. The scatters of models in high PDF region are very small such that the mean model parameters will be very close to the actual model parameters when q is fixed (Fig. 9b). From the cross-plots (Fig. 9) and Table 1a, it can also be concluded that there is no uncertainty in determination of z; however, there is uncertainty in the model parameter k as there is a large variation. However, cross-plot between k, z and q is presented in Fig. 10a and reveals a similar nature for noisy data where models having misfit less than the threshold (0.01 for 10% random noisy data) (grey), and models with high PDF (black) when q is free. Fig. 10b reveals that scatter is large for noisy data but models

Table 3b
Actual model parameters, search range and interpreted mean model for noise free, 20% Gaussian noise with uncertainty for vertical cylinder (Model 3b).

Model parameters	Actual value	Search range	Mean model (noise-free)		Mean model (noisy data)	
			q variable	q fixed	q variable	q fixed
k (mGal × m)	−300	−500–0	−294.7 ± 14.9	−299.9 ± 0.8	−496.7 ± 9.9	−310.3 ± 1.9
x_0 (m)	300	100–500	300.0 ± 0.1	300.0 ± 0.0	300.9 ± 0.6	301.3 ± 0.5
z (m)	70	0–100	69.6 ± 1.1	70.0 ± 0.2	70.6 ± 0.7	61.6 ± 0.6
q	0.5	0–2	0.51 ± 0.0	0.50 (fixed)	0.56 ± 0.0	0.50 (fixed)
Misfit			9.2×10^{-7}	4.9×10^{-8}	1.4×10^{-2}	1.4×10^{-3}

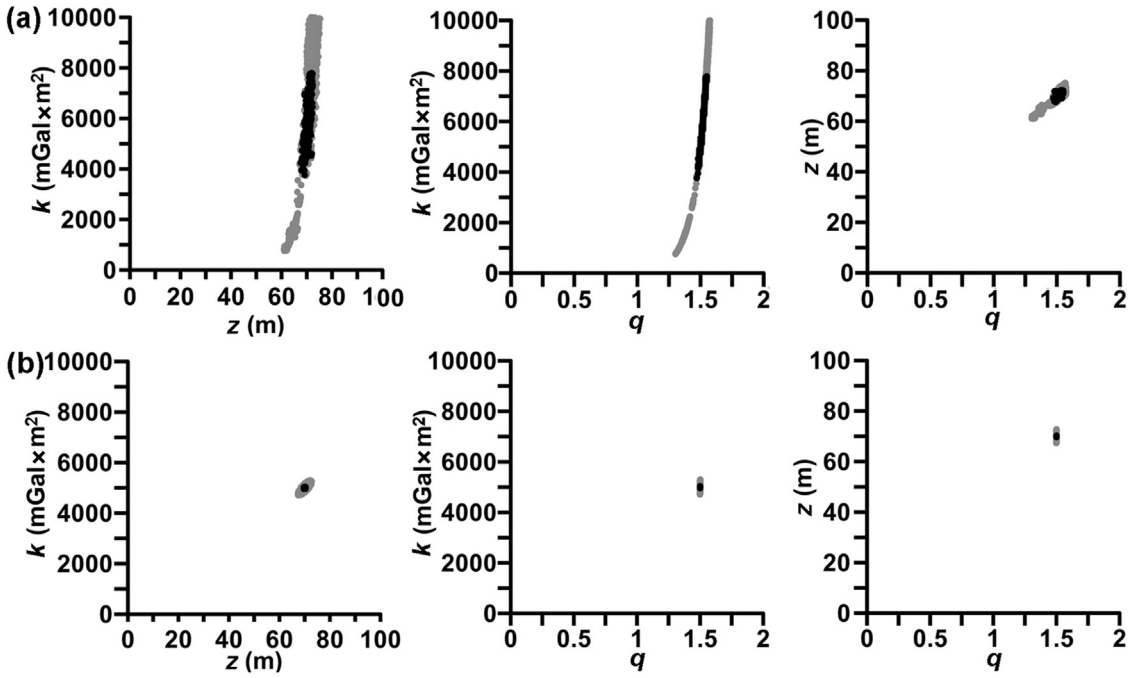

Figure 9. (a) Cross-plots between amplitude coefficient (k), depth (z), shape factor (q) for all models having misfit < threshold (10^{-4} for noise-free data) (grey), and models with PDF >60.65% (black) when q is free for sphere (Model 1a); (b) cross-plots between amplitude coefficient (k), depth (z), shape factor (q) for all models having misfit < threshold (10^{-4} for noise-free data) (grey), and models with PDF >60.65% (black) when q is fixed for sphere (Model 1a).

in high PDF region are restricted near the actual value when q is fixed.

4.2.2. Horizontal cylinder (noise free and 20% Gaussian noisy — Model 2b)

The cross-plots depict similar situation like Model 1a and are shown in Fig. 11. The model parameters k, z, and q using accepted models with misfit lower than 10^{-4} (grey) and models within the pre-defined high PDF region (black) when q is free. The cross-plot between k, z and q is also examined and reveals a similar nature like noise free data when shape factor is free and fixed (Fig. 11a and b) and Gaussian noisy data (Fig. 12a and b). However, in this model, the scatter is less for noisy Gaussian data as compared to random noisy data. Figs. 11b and 12b reveal that the models in high PDF

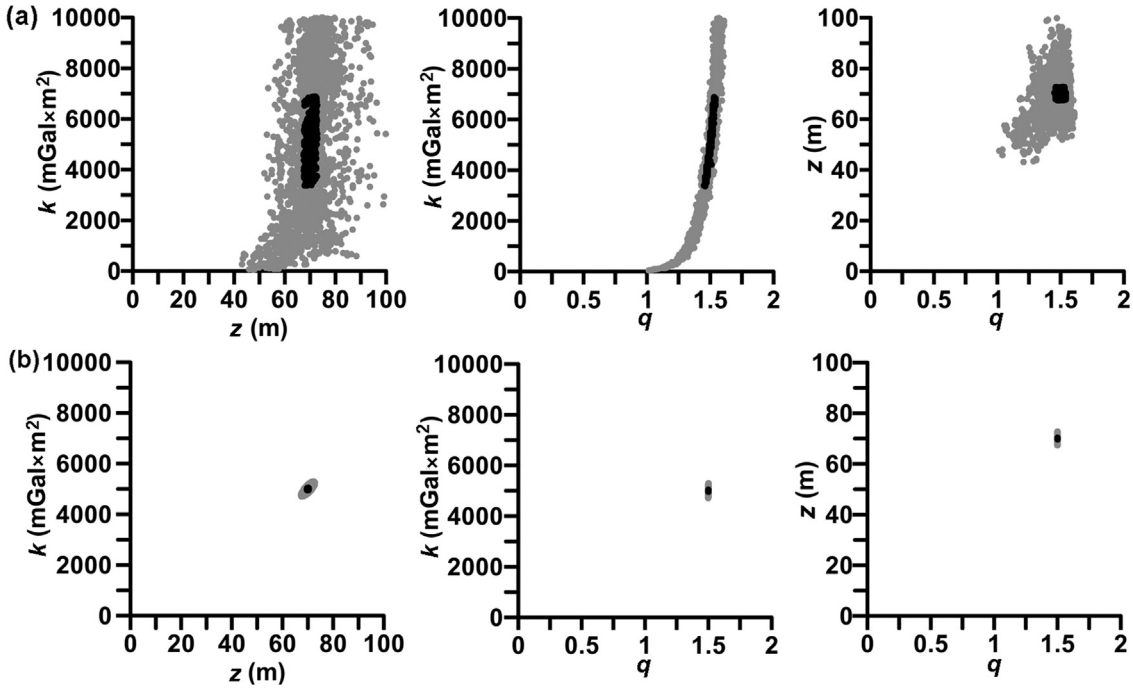

Figure 10. (a) Cross-plots between amplitude coefficient (k), depth (z), shape factor (q) for all models having misfit < threshold (0.01 for 10% random noisy data) (grey), and models with PDF >60.65% (black) when q is free for sphere (Model 1a); (b) cross-plots between amplitude coefficient (k), depth (z), shape factor (q) for all models having misfit < threshold (0.01 for 10% random noisy data) (grey), and models with PDF >60.65% (black) when q is fixed for sphere (Model 1a).

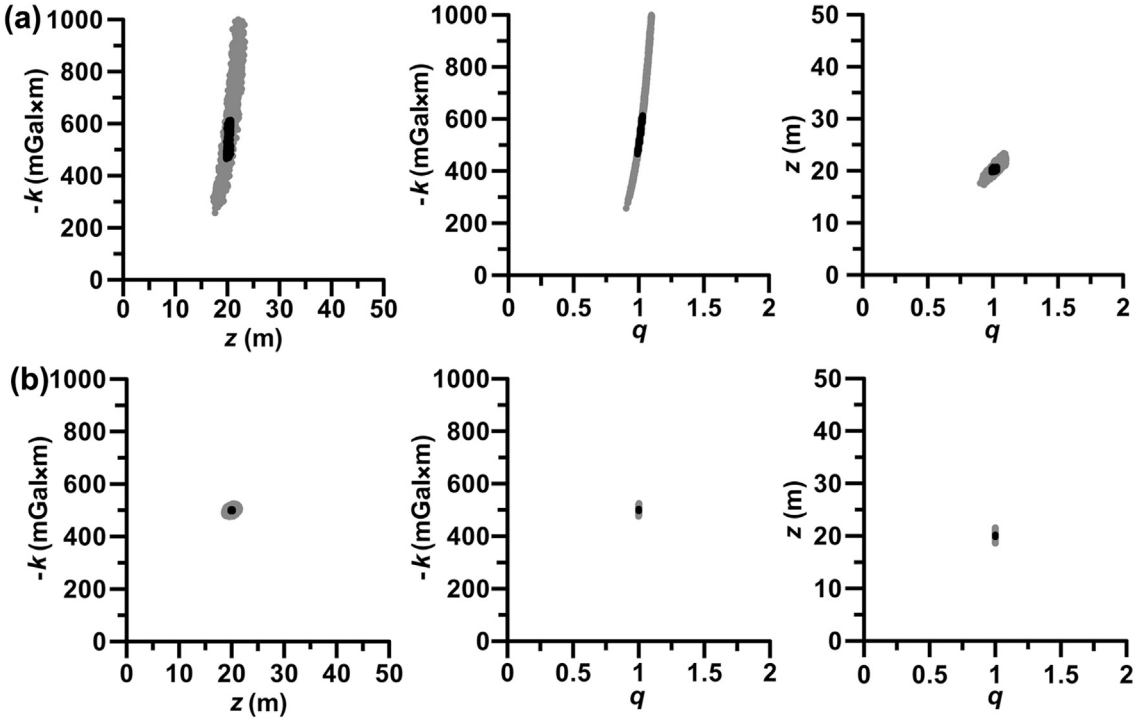

Figure 11. (a) Cross-plots between amplitude coefficient (k), depth (z), shape factor (q) for all models having misfit < threshold (10^{-4} for noise-free data) (grey), and models with PDF >60.65% (black) when q is free for horizontal cylinder (Model 2a); (b) cross-plots between amplitude coefficient (k), depth (z), shape factor (q) for all models having misfit < threshold (10^{-4} for noise-free data) (grey), and models with PDF >60.65% (black) when q is fixed for horizontal cylinder (Model 2a).

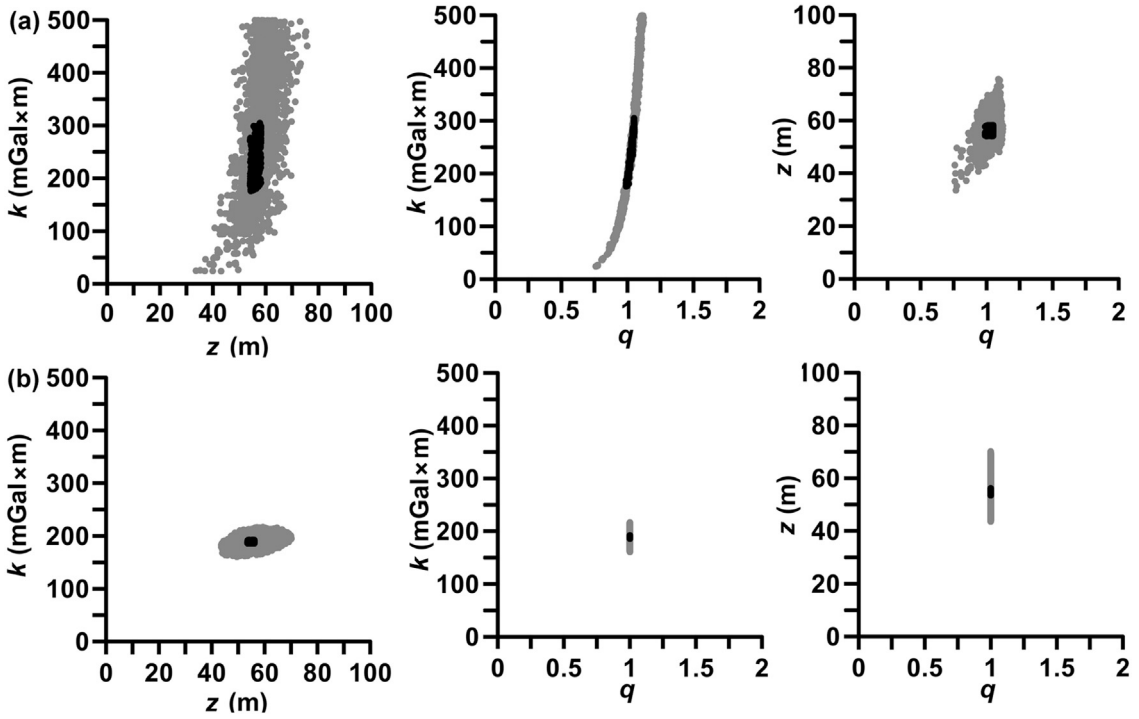

Figure 12. (a) Cross-plots between amplitude coefficient (k), depth (z), shape factor (q) for all models having misfit < threshold (0.01 for 20% Gaussian noisy data) (grey), and models with PDF >60.65% (black) when q is free for horizontal cylinder (Model 2b); (b) cross-plots between amplitude coefficient (k), depth (z), shape factor (q) for all models having misfit < threshold (0.01 for 20% Gaussian noisy data) (grey), and models with PDF >60.65% (black) when q is fixed for horizontal cylinder (Model 2b).

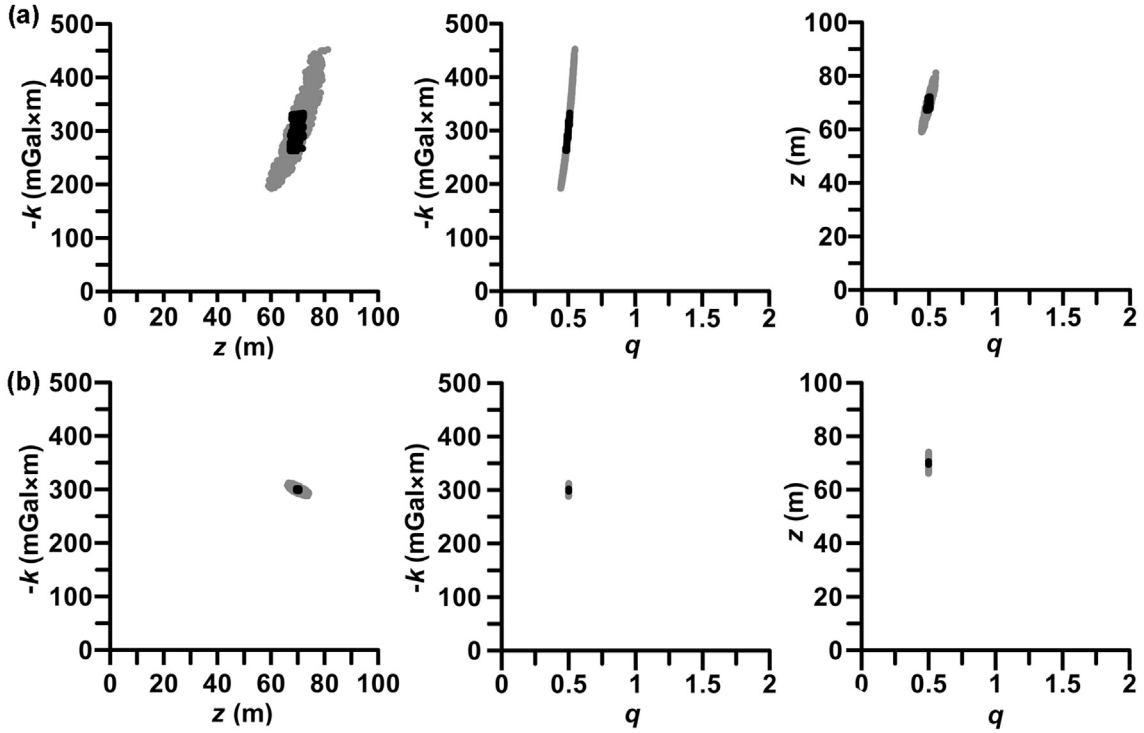

Figure 13. (a) Cross-plots between amplitude coefficient (k), depth (z), shape factor (q) for all models having misfit < threshold (10^{-4} for noise-free data) (grey), and models with PDF >60.65% (black) when q is free for vertical cylinder (Model 3b); (b) cross-plots between amplitude coefficient (k), depth (z), shape factor (q) for all models having misfit < threshold (10^{-4} for noise-free data) (grey), and models with PDF >60.65% (black) when q is fixed for vertical cylinder (Model 3b).

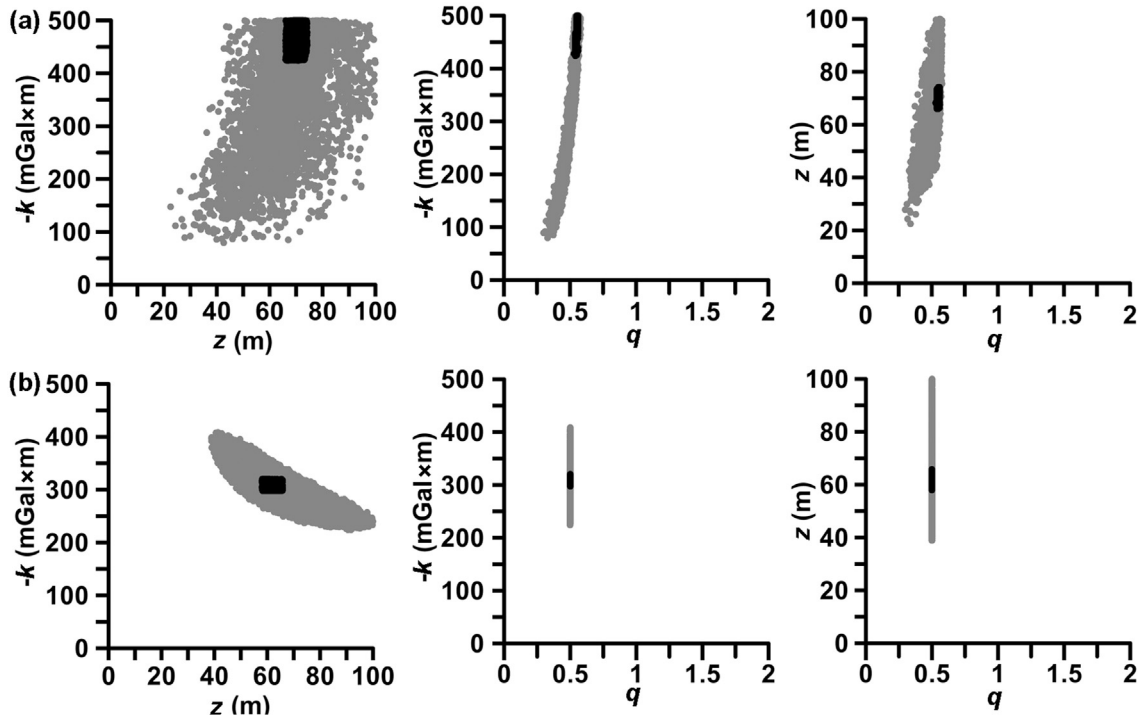

Figure 14. (a) Cross-plots between amplitude coefficient (k), depth (z), shape factor (q) for all models having misfit < threshold (0.01 for 20% Gaussian noisy data) (grey), and models with PDF >60.65% (black) when q is free for vertical cylinder (Model 3b); (b) cross-plots between amplitude coefficient (k), depth (z), shape factor (q) for all models having misfit < threshold (0.01 for 20% Gaussian noisy data) (grey), and models with PDF >60.65% (black) when q is fixed for vertical cylinder (Model 3b).

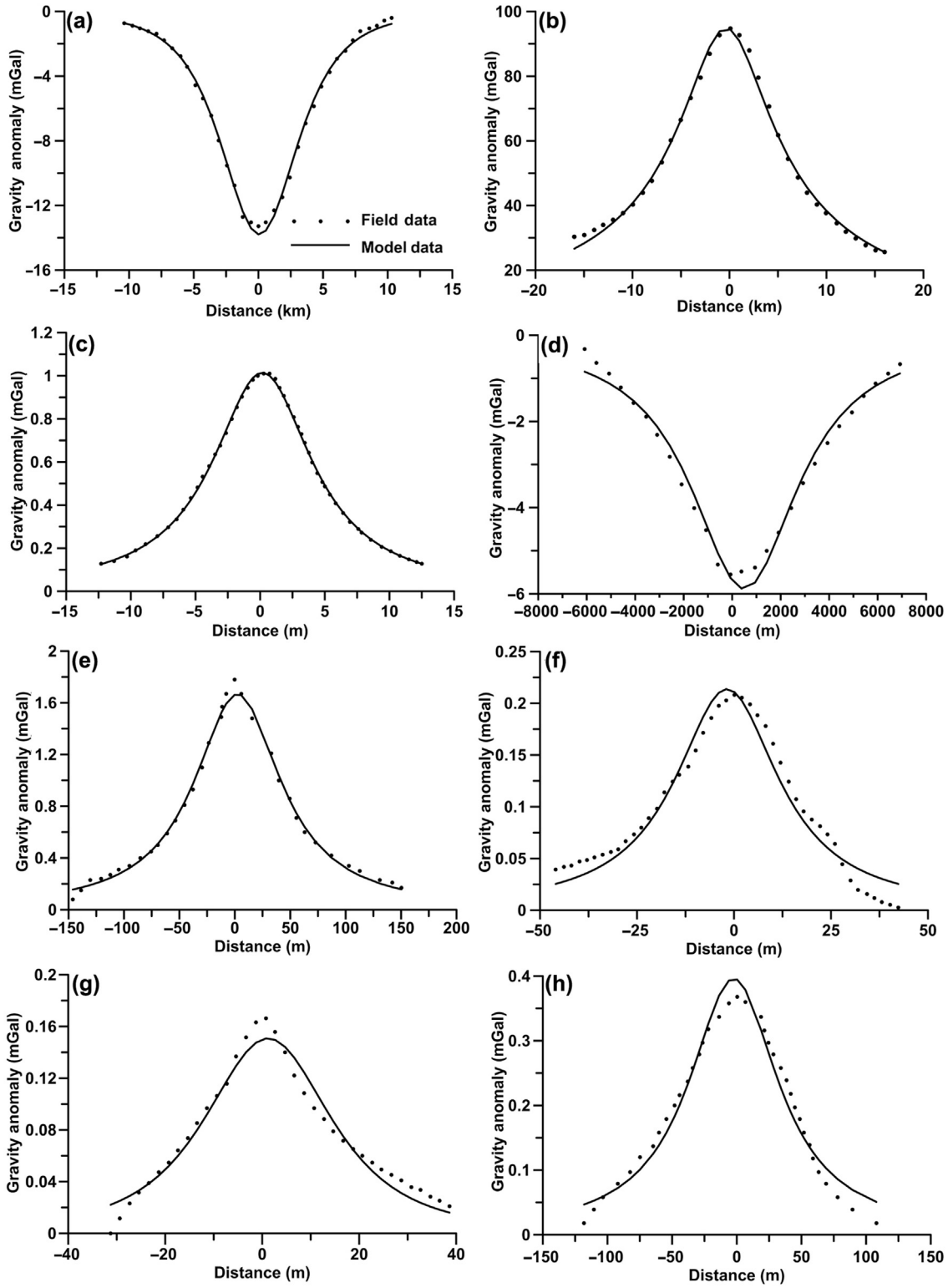

Figure 15. Fittings between the field and model data for (a) Humble dome anomaly, Houston, Texas, USA; (b) Leona anomaly, South Saint-Louis, western coastline, Senegal; (c) The Karrbo gravity anomaly, Sweden; (d) Offshore Louisiana Salt dome anomaly, USA; (e) Mobrun anomaly, Noranda, Quebec, Canada; (f) Camaguey Province anomalies, Cuba (Profile 1); (g) Camaguey Province anomalies, Cuba (Profile 2); (h) Camaguey Province anomalies, Cuba (Profile 3).

Table 4
Search range and interpreted mean model for Humble dome anomaly, Houston, Texas, USA.

Model parameters	Search range	Mean model (VFSA)	Tlas et al. (2005)	Asfahani and Tlas (2012)	Mehanee (2014)
k (mGal × km^2)	−500–0	−275.6 ± 2.5	−283.14	−279.81	−292.54
x_0 (km)	−5–5	0.07 ± 0.0	0.01	–	–
z (km)	0–50	4.4 ± 0.0	4.59	4.58	4.62
q	1.5	1.5	1.47	1.48	1.5
Misfit		9.1×10^{-4}	–	–	4.8%

region (black) are restricted near the actual value of the model parameters when q is fixed.

4.2.3. Vertical cylinder (noise free and 20% Gaussian noisy – Model 3b)

The cross-plots depict similar situation like Model 1a and 2b (Fig. 13a) when q is free. The scatters of models in high PDF region are very small such that the mean model parameters will be very close to the actual model parameters when q is fixed (Fig. 13b). The noisy data reveals the same as discussed for Model 1a and 2b and are shown in Fig. 14a and b.

From the theoretical studies carried out for gravity anomaly using noise-free and noisy synthetic data for a sphere, horizontal and vertical cylinder, it can be concluded that, in order to obtain a reliable result, the shape factor q should be fixed and other three model parameters must be optimized. The shape factor q can be obtained using a test run by optimizing it between 0–2. It is highlighted that when q is also a variable, uncertainty in the estimation of other model parameters are high; especially k shows a huge uncertainty with high misfit. Moreover, horizontal location and depth are determined judiciously well (Tables 1a, 2a and 3a) with some uncertainty, even when q is variable. Further, when q is fixed, all model parameters are determined exactly well with very small uncertainty. This is also supported by the analysis of cross-plots as discussed. Therefore, optimization with fixed q is highlighted here in the study. Further, correlation matrices reveal similar nature for sphere, horizontal cylinder and vertical cylinders. A very strong correlation between various model parameters is observed when q is also a variable. This indicates that parameters are interdependent and cannot be resolved very well. However, correlation between various parameters becomes very small when q is fixed, highlighting model well resolved parameters.

4.3. Field example

To demonstrate the efficiency of the approach eight field example of residual gravity anomaly from different parts of the world is considered. Here, it should be stated that with minor change in q, k and z changes considerably. With decrease in q, k decreases and increase of q increases k as observed in the standard geometrical models. Moreover, field data is often associated with noise and in common, exact shape of sphere, cylinder or sheet cannot be found in geological nature. Therefore, field data cannot be fitted precisely well with the model response from simple shaped targets. Hence, q shall be variable if there is irregular shaped body which is closer to the actual or true structure.

4.3.1. Humble dome anomaly, Houston, Texas, USA

The residual gravity anomaly map over the Humble dome near Houston, Texas was taken after Nettleton (1976) and is shown in Fig. 15a. This anomaly has been interpreted by several authors (Shaw and Agarwal, 1990; Abdelrahman et al., 2001a; Salem et al., 2003, 2004; Tlas et al., 2005; Asfahani and Tlas, 2012; Mehanee, 2014) assuming a spherical structure. The observed anomaly is obtained by digitizing at 610 m interval from above mentioned published literature (Fig. 15a) and interpreted using VFSA optimization.

Initially, a suitable search range (Table 4) for each model parameter is selected. Next, a single VFSA run is performed and the convergence of each model parameter and reduction of misfit is analysed. Afterwards, 10 VFSA runs are performed and 10 solutions are derived. Initial interpretation yields shape factor 'q' as 1.52 and this suggests a 3-D spherical type model. Subsequently, q is fixed at 1.5 and optimization is repeated. Once again 10 VFSA runs are performed; models with misfit 0.01 are selected to compute PDF. Models in high PDF region (one standard deviation) are used to compute the mean model and associated uncertainty. Table 4 presents the interpreted model parameters and uncertainty as well as comparison with other recently published results.

The depth of the body estimated in the present study is 4.4 km and is quite excellent with the other results. The depth obtained by Tlas et al. (2005) ($z = 4.59$ km), using adaptive simulated annealing, Asfahani and Tlas (2012) ($z = 4.58$ km), using flair function minimization and Mehanee (2014) ($z = 4.62$ km) using regularised inversion in interpretation of residual gravity anomaly. A comparison of interpretation results by various methods reveals that present approach is in good agreement with other interpretation methods. However, the misfit is less compared to the previous study as shown in Table 4. The amplitude coefficient k and the location of the body x_0 are also a very important parameters and this should also be determined with other model parameters also. A qualitative knowledge about the nature of structure can be made using the best estimate of k from the present approach. A comparison between the field data and modelled data is shown in Fig. 15a.

4.3.2. Leona anomaly, South Saint-Louis, Western Coastline, Senegal

The residual gravity anomaly of west coast of Senegal in West Africa (Nettleton, 1976) was taken for a profile length of 30 km and is shown in Fig. 15b. The anomaly is digitized with an equal interval of 500 m. This anomaly was also interpreted by several authors as spherical structure (Tlas et al., 2005; Asfahani and Tlas, 2012; Mehanee, 2014). A two-step inversion is performed after selecting suitable search range for each model parameter. In the first step, value of q is estimated as 0.54 which points towards a vertical cylindrical structure. Subsequently, q is fixed at 0.50 and optimization procedure is repeated. Table 5 depicts the interpreted model parameters and comparison with other published results. The depth of the body estimated in the present study is 4.6 km. The depth obtained by Tlas et al. (2005) ($z = 9.17$ km), using adaptive simulated annealing, Asfahani and Tlas (2012) ($z = 9.13$ km), using flair function minimization and Mehanee (2014) ($z = 12.2$ km) using regularised inversion in interpretation of residual gravity anomaly. However, the estimated depth and the geometrical body interpreted by the other authors are considered as sphere. In the present study, it is found that the shape factor is pointing towards a vertical cylinder and interpreted the same. Table 5 depicts that Mehanee (2014) also interpreted the same anomaly as vertical cylinder as well where the depth is estimated as 4.59 km. However, the misfit for vertical cylinder is less compared to sphere. In the present study, the anomaly is interpreted as vertical cylinder. The misfit computed from the present study is less compared to other methods. A comparison of interpretation results by various methods also reveals that present approach is in good agreement with the interpretation methods for vertical cylindrical structure. A comparison between the field data and modelled data is shown in Fig. 15b.

Table 5
Search range and interpreted mean model for Leona anomaly, South Saint-Louis, western Coastline, Senegal.

Model parameters	Search range	Mean model (VFSA)	Tlas et al. (2005)	Asfahani and Tlas (2012)	Mehanee (2014) (sphere)	Mehanee (2014) (vertical cylinder)
k (mGal × km)	10–200	94.7 ± 0.7	6971.83 mGal × km^2	6931.78 mGal × km^2	13026.03 mGal × km^2	436.31
x_0 (km)	−5–5	−0.4 ± 0.0	0.22	–	–	–
z (km)	0–20	4.6 ± 0.0	9.17	9.13	12.2	4.59
q	0.5	0.5	1.499	1.499	1.5	0.5
Misfit		3.8 × 10^{-4}	–	–	8.9%	3.5%

Table 6
Search range and interpreted mean model for the Karrbo gravity anomaly, Sweden.

Model parameters	Search range	Mean model (VFSA)	Tlas et al. (2005)	Asfahani and Tlas (2012)
k (mGal × m)	0–20	4.76 ± 0.0	5.27	5.23
x_0 (m)	−5–5	0.2 ± 0.0	0.18	–
z (m)	0–20	4.7 ± 0.0	4.82	4.84
q	1.0	1.0	1.02	1.02
Misfit		4.6 × 10^{-5}	–	–

Table 8
Search range and interpreted mean model for Mobrun anomaly, Noranda, Quebec, Canada.

Model parameters	Search range	Mean model (VFSA)	Mehanee (2014)
k (mGal × m)	0–100	79.5 ± 0.7	80
x_0 (m)	−5–5	2.5 ± 0.4	–
z (m)	0–60	47.7 ± 0.6	47
q	1.0	1.0	1.0
Misfit		6.5 × 10^{-4}	5.9%

4.3.3. The Karrbo gravity anomaly, Sweden

A residual gravity anomaly map at Karrbo, Vastmanland, Sweden was measured over the pyrrhotite ore body. The length of the profile was measured for 25.6 m (Shaw and Agarwal, 1990) is shown in Fig. 15c. The interpretation of this residual anomaly is carried out by applying the VFSA technique and assuming a variable geometric shape factor q of the responsible buried body. The first step optimization yields shape factor 1.01 when q is also optimized with other model parameter. This reveals that this anomaly can be fitted with a horizontal cylindrical model. Next, q is fixed to 1.0 and optimization is performed. The interpreted results are shown in Table 6. Fig. 15c depicts the fitting between the observed and interpreted mean model response. The depth of the body estimated in the present study is 4.7 m. The depth obtained by Tlas et al. (2005) (z = 4.82 m), using adaptive simulated annealing, Asfahani and Tlas (2012) (z = 4.84 m). The results are also in good agreement with the other results. The misfit is estimated as quite low. A comparison between the field data and modelled data is shown in Fig. 15c.

4.3.4. Offshore Louisiana Salt dome anomaly, USA

A residual gravity map over a salt dome, offshore Louisiana, USA (Nettleton, 1976; Roy et al., 2000) was taken and is shown in Fig. 15d. A two-step interpretation procedure is again carried out in this field data and it shows that the shape factor is pointing towards horizontal cylinder. Next, the shape factor is fixed at 1.0 and the VFSA procedure is repeated again. The interpreted results are shown in Table 7. Fig. 15d depicts the fitting between the observed and interpreted mean model response. The depth of the body estimated in the present study is 2702.2 m. The depth obtained by Mehanee (2014) using flair function minimization is 2899 m. Again the misfit obtained by the present method is less compared to the other method.

4.3.5. Mobrun anomaly, Noranda, Quebec, Canada

A residual gravity anomaly map of Noranda mining district, Quebec, Canada was taken (Siegel et al., 1957; Grant and West, 1965; Roy et al., 2000) over a massive sulphide ore body (Fig. 15e). A two-step interpretation procedure is again carried out in this field data and it shows that the shape factor is pointing towards horizontal cylinder. Next, the shape factor is fixed at 1.0 and the VFSA procedure is repeated again. The interpreted results are shown in Table 8. Fig. 15e depicts the fitting between the observed and interpreted mean model response. The depth of the body estimated in the present study is 47.7 m and is in excellent agreement with the depth obtained by Mehanee (2014) using flair function minimization as 47 m. Also, the misfit in the present approach is quite low as compared to other method.

4.3.6. Camaguey Province anomalies, Cuba

A detailed gravity surveys were completed in the Camaguey Province, Cuba for the prospecting of chromite deposits (Davis et al., 1957). Residual gravity anomaly maps were taken over many spatially disseminated chromite ore bodies and also from the disclosed later from drilling results and the intrusive dense bodies in the area. In this field example, three profiles from this area are taken and interpreted using the present method. Profiles 1 and 2 overlie a chromite ore body, while Profile 3 overlies an intrusive dense body. These profiles were digitized at an equal interval of about 2 m.

In the first profile (Profile 1); Fig. 15f, a two-step interpretation procedure is again carried out in this field data and it shows that the shape factor is pointing towards horizontal cylinder. Next, the shape factor is fixed and the VFSA procedure is repeated again. The interpreted results are shown in Table 9. Fig. 15f depicts the fitting between the observed and interpreted mean model response. The depth of the body estimated in the present study is 16.2 m and is in

Table 7
Search range and interpreted mean model for Offshore Louisiana Salt dome anomaly, USA.

Model parameters	Search range	Mean model (VFSA)	Mehanee (2014)
k (mGal × m)	0–100,000	16,021 ± 131.0	16,400
x_0 (m)	−50–1000	506.5 ± 18.4	-
z (m)	100–3000	2702.2 ± 21.5	2899
q	1.0	1.0	1.0
Misfit		2.9 × 10^{-3}	12.4%

Table 9
Search range and interpreted mean model for Camaguey Province anomalies, Cuba (Profile 1).

Model parameters	Search range	Mean model (VFSA)	Mehanee (2014)
k (mGal × m)	0–50	3.5 ± 0.0	3
x_0 (m)	−5–5	−1.8 ± 0.0	-
z (m)	0–50	16.2 ± 0.0	16
q	1.0	1.0	1.0
Misfit		8.1 × 10^{-3}	12.1%

Table 10
Search range and interpreted mean model for Camaguey Province anomalies, Cuba (Profile 2).

Model parameters	Search range	Mean model (VFSA)	Mehanee (2014)
K (mGal × m^2)	0–200	61.2 ± 0.5	61
x_0 (m)	−5–5	1.2 ± 0.0	-
z (m)	0–50	20.2 ± 0.1	20
q	1.5	1.5	1.5
Misfit		4.9×10^{-3}	10.1%

Table 11
Search range and interpreted mean model for Camaguey Province anomalies, Cuba (Profile 3).

Model parameters	Search range	Mean model (VFSA)	Mehanee (2014)
K (mGal × m^2)	0–50	16.8 ± 0.1	18
x_0 (m)	−5–5	−2.4 ± 0.3	-
z (m)	0–100	42.3 ± 0.4	47
q	1.0	1.0	1.5
Misfit		4.4×10^{-3}	8.5%

excellent agreement with the depth obtained by Mehanee (2014) using flair function minimization as 16 m.

The second profile (Profile 2); Fig. 15g, the inversion procedure is repeated and found to be a spherical type structure. The interpreted results are shown in Table 10. Fig. 15g depicts the fitting between the observed and interpreted mean model response. The depth of the body estimated in the present study is 20.2 m and is in excellent agreement with the depth obtained by Mehanee (2014) using flair function minimization as 20 m.

The third profile (Profile 3); Fig. 15h, the inversion procedure is repeated and found to be a horizontal cylindrical type structure. The interpreted results are shown in Table 11. Fig. 15h depicts the fitting between the observed and interpreted mean model response. The depth of the body estimated in the present study is 42.3 m and is in fair agreement with the depth obtained by Mehanee (2014) using flair function minimization as 47 m.

It should be highlighted that a comparison of Tables 4 to 11 reveals that most authors do not consider horizontal location 'x_0' of the body as a model parameter. This means they consider origin as the location of the body. This is not accurate always. A small improper estimate in any model parameter can affect other model parameters as well. Possibly this could be the main reason for different estimates of model parameter in Table 4 to 11 by different authors. However, in the present approach, the misfit or error is less compared to other methods as discussed.

5. Conclusions

A proficient method is utilized for the interpretation of residual gravity anomaly using a VFSA global optimization method. As VFSA is able to find a number of good-fitting models in a huge multi-dimensional model space, the nature of uncertainty in the interpretation has also been examined simultaneously. The present study discloses that, while optimizing all model parameters (amplitude coefficient, depth and shape factor) together, the VFSA approach yields a number of equivalent solutions. It has been observed that the shape factor plays an important role in finding a reliable estimate of other model parameters. The analysis of uncertainty shows that a small change in the shape factor produces a large change in the estimated amplitude coefficient (k). Hence, inaccurate estimates of other model parameters have also been obtained. It has been perceived that the optimization method is able to decide all the model parameters accurately when shape factor is fixed to its actual value. Therefore, interpretation of gravity anomaly data is carried out by adjusting a two-step inversion. Firstly, all the model parameters are optimized and the parameters are studied. Next, the inversion results obtained after the first step directs the value of shape factor around 1.5, 1.0 or 0.5. Then, in the second step, the shape factor is fixed to 1.5, 1.0 or 0.5 and other model parameters are optimized and the most reliable result has been obtained and uncertainty in the interpretation has also become irrelevant. Therefore, the mean model computed from the models lying in the high Probability Density Function (PDF) region (with one standard deviation) gives the most reliable results with the least uncertainty. The efficacy of this approach is demonstrated using noise-free and noisy synthetic data and field examples. The computation time of two step procedure is very short. The actual (not CPU) time for the whole computation process for one step solution is nearly 20 s. It is highlighted that even if the shape factor is known either from a priori geological information or anomaly contour map, interpretation should be performed in two steps to obtain the most reliable estimation of various model parameters as well as actual validation of geometrical shape of the subsurface structure.

Acknowledgements

The author would like to thank the Editor-in-chief Prof. Xuanxue Mo, Co-editor-in-chief Prof. M. Santosh, and Associate Editor Dr. Yener Eyuboglu for the review. The author also likes to thank Dr. Nafiz Maden and the anonymous reviewers for their suggestions which have immensely improved the quality of the manuscript. This work is a tribute to the author's Ph.D supervisor Prof. Shashi Prakash Sharma, Geology and Geophysics, IIT Kharagpur. The author would also like to thank the Director of IISER Bhopal for providing the necessary facilities to complete this work.

References

Abdelrahman, E.M., El-Araby, T.M., El-Araby, H.M., Abo-Ezz, E.R., 2001a. Three least squares minimization approaches to depth, shape, and amplitude coefficient determination from gravity data. Geophysics 66, 1105–1109.
Abdelrahman, E.M., El-Araby, T.M., El-Araby, H.M., Abo-Ezz, E.R., 2001b. A new method for shape and depth determinations from gravity data. Geophysics 66, 1774–1780.
Abdelrahman, E.M., Sharafeldin, S.M., 1995a. A least-squares minimization approach to depth determination from numerical horizontal gravity gradients. Geophysics 60, 1259–1260.
Abdelrahman, E.M., Sharafeldin, S.M., 1995b. A least-squares minimization approach to shape determination from gravity data. Geophysics 60, 589–590.
Abdelrahman, E.M., El-Araby, T.M., 1993. A least-squares minimization approach to depth determination from moving average residual gravity anomalies. Geophysics 59, 1779–1784.
Abdelrahman, E.M., Bayoumi, A.I., El-Araby, H.M., 1991. A least-squares minimization approach to invert gravity data. Geophysics 56, 115–118.
Abdelrahman, E.M., 1990. Discussion on "A least-squares approach to depth determination from gravity data" by Gupta, O.P. Geophysics 55, 376–378.
Abdelrahman, E.M., Bayoumi, A.I., Abdelhady, Y.E., Gobash, M.M., EL-Araby, H.M., 1989. Gravity interpretation using correlation factors between successive least-squares residual anomalies. Geophysics 54, 1614–1621.
Asfahani, J., Tlas, M., 2012. Fair function minimization for direct interpretation of residual gravity anomaly profiles due to spheres and cylinders. Pure and Applied Geophysics 169, 157–165.
Beck, R.H., Qureshi, I.R., 1989. Gravity mapping of a subsurface cavity at Marulan, N.S.W. Exploration Geophysics 20, 481–486.
Biswas, A., Sharma, S.P., 2015. Interpretation of self-potential anomaly over idealized body and analysis of ambiguity using very fast simulated annealing global optimization. Near Surface Geophysics 13 (2), 179–195. http://dx.doi.org/10.3997/1873-0604.2015005.
Biswas, A., Sharma, S.P., 2014a. Resolution of multiple sheet-type structures in self-potential measurement. Journal of Earth System Science 123 (4), 809–825.
Biswas, A., Sharma, S.P., 2014b. Optimization of self-potential interpretation of 2-D inclined sheet-type structures based on very fast simulated annealing and analysis of ambiguity. Journal of Applied Geophysics 105, 235–247.
Bowin, C., Scheer, E., Smith, W., 1986. Depth estimates from ratios of gravity, geoid and gravity gradient anomalies. Geophysics 51, 123–136.
Davis, W.E., Jackson, W.H., Richter, D.H., 1957. Gravity prospecting for chromite deposits in Camaguey province, Cuba. Geophysics 22 (4), 848–869.

Dosso, S.E., Oldenburg, D.W., 1991. Magnetotelluric appraisal using simulated annealing. Geophysical Journal International 106, 370–385.
Elawadi, E., Salem, A., Ushijima, K., 2001. Detection of cavities from gravity data using a neural network. Exploration Geophysics 32, 75–79.
Essa, K.S., 2007. Gravity data interpretation using the s-curves method. Journal of Geophysics and Engineering 4 (2), 204–213.
Essa, K.S., 2012. A fast interpretation method for inverse modelling of residual gravity anomalies caused by simple geometry. Journal of Geological Research Volume 2012. Article ID 327037.
Essa, K.S., 2014. New fast least-squares algorithm for estimating the best-fitting parameters due to simple geometric-structures from gravity anomalies. Journal of Advanced Research 5 (1), 57–65. http://dx.doi.org/10.1016/j.jare.2012.11.006.
Fedi, M., 2007. DEXP: a fast method to determine the depth and the structural index of potential fields sources. Geophysics 72 (1), I1–I11.
Grant, F.S., West, G.F., 1965. Interpretation Theory in Applied Geophysics. McGraw-Hill Book Co.
Gupta, O.P., 1983. A least-squares approach to depth determination from gravity data. Geophysics 48, 360–375.
Hartmann, R.R., Teskey, D., Friedberg, I., 1971. A system for rapid digital aeromagnetic interpretation. Geophysics 36, 891–918.
Hinze, W.J., 1990. The role of gravity and magnetic methods in engineering and environmental studies. In: Ward, S.H. (Ed.), Geotechnical and Environmental Geophysics, Review and Tutorial, Vol. I. Society of Exploration Geophysicists, Tulsa, OK.
Hinze, W.J., Von Frese, R.R.B., Saad, A.H., 2013. Gravity and Magnetic Exploration: Principles, Practices and Applications. Cambridge University Press, New York, USA.
Jain, S., 1976. An automatic method of direct interpretation of magnetic profiles. Geophysics 41, 531–541.
Juan, L.F.M., Esperanza, G., José, G.P.F.Á., Heidi, A.K., César, O.M.P., 2010. PSO: a powerful algorithm to solve geophysical inverse problems: application to a 1D-DC resistivity case. Journal of Applied Geophysics 71, 13–25.
Kilty, T.K., 1983. Werner deconvolution of profile potential field data. Geophysics 48, 234–237.
Lafehr, T.R., Nabighian, M.N., 2012. Fundamentals of Gravity Exploration. Society of Exploration Geophysicists, Tulsa, Ok., USA.
Lines, L.R., Treitel, S., 1984. A review of least-squares inversion and its application to geophysical problems. Geophysical Prospecting 32, 159–186.
Long, L.T., Kaufmann, R.D., 2013. Acquisition and Analysis of Terrestrial Gravity Data. Cambridge University Press, New York, USA.
Mehanee, S.A., 2014. Accurate and efficient regularised inversion approach for the interpretation of isolated gravity anomalies. Pure and Applied Geophysics 171, 1897–1937. http://dx.doi.org/10.1007/s00024-013-0761-z.
Mohan, N.L., Anandababu, L., Roa, S., 1986. Gravity interpretation using the Melin transform. Geophysics 51, 114–122.
Mosegaard, K., Tarantola, A., 1995. Monte Carlo sampling of solutions to inverse problems. Journal of Geophysical Research 100 (B7), 12431–12447.
Nettleton, L.L., 1962. Gravity and magnetics for geologists and seismologists. AAPG 46, 1815–1838.
Nettleton, L.L., 1976. Gravity and Magnetics in Oil Prospecting. McGraw-Hill Book Co.
Odegard, M.E., Berg, J.W., 1965. Gravity interpretation using the Fourier integral. Geophysics 30, 424–438.
Rothman, D.H., 1985. Nonlinear inversion, statistical mechanics and residual statics estimation. Geophysics 50, 2784–2796.
Rothman, D.H., 1986. Automatic estimation of large residual statics correction. Geophysics 51, 337–346.
Roy, A., 1966. The method of continuation in mining geophysical interpretation. Geoexploration 4, 65–83.
Roy, L., Agarwal, B.N.P., Shaw, R.K., 2000. A new concept in Euler deconvolution of isolated gravity anomalies. Geophysical Prospecting 48, 559–575.
Salem, A., Ravat, D., 2003. A combined analytic signal and Euler method (AN-EUL) for automatic interpretation of magnetic data. Geophysics 68 (6), 1952–1961.
Salem, A., Elawadib, E., Ushijima, K., 2003. Depth determination from residual gravity anomaly data using a simple formula. Computers & Geosciences 29, 801–804.
Salem, A., Ravat, D., Mushayandebvu, M.F., Ushijima, K., 2004. Linearized least-squares method for interpretation of potential-field data from sources of simple geometry. Geophysics 69 (3), 783–788.
Sen, M.K., Stoffa, P.L., 2013. Global Optimization Methods in Geophysical Inversion, second ed. Cambridge Publisher, London.
Sharma, S.P., 2012. VFSARES – a very fast simulated annealing FORTRAN program for interpretation of 1-D DC resistivity sounding data from various electrode array. Computers & Geosciences 42, 177–188.
Sharma, S.P., Biswas, A., 2011. Global nonlinear optimization for the estimation of static shift and interpretation of 1-D magnetotelluric sounding data. Annals of Geophysics 54 (3), 249–264.
Sharma, S.P., Biswas, A., 2013. Interpretation of self-potential anomaly over a 2D inclined structure using very fast simulated-annealing global optimization – an insight about ambiguity. Geophysics 78, WB3–WB15.
Sharma, B., Geldart, L.P., 1968. Analysis of gravity anomalies of two-dimensional faults using Fourier transforms. Geophysical Prospecting 16, 77–93.
Sharma, S.P., Kaikkonen, P., 1998. Two-dimensional nonlinear inversion of VLF-R data using simulated annealing. Geophysical Journal International 133, 649–668.
Sharma, S.P., Kaikkonen, P., 1999a. Appraisal of equivalence and suppression problems in 1-D EM and DC measurements using global optimization and joint inversion. Geophysical Prospecting 47, 219–249.
Sharma, S.P., Kaikkonen, P., 1999b. Global optimisation of time domain electromagnetic data using very fast simulated annealing. Pure and Applied Geophysics 155, 149–168.
Sharma, S.P., Verma, S.K., 2011. Solutions of the inherent problem of the equivalence in direct current resistivity and electromagnetic methods through global optimization and joint inversion by successive refinement of model space. Geophysical Prospecting 59, 760–776.
Shaw, R.K., Agarwal, B.N.P., 1990. The application of Walsh transforms to interpret gravity anomalies due to some simple geometrically shaped causative sources: a feasibility study. Geophysics 55, 843–850.
Sen, M.K., Stoffa, P.L., 1996. Bayesian inference, Gibbs sampler and uncertainty estimation in geophysical inversion. Geophysical Prospecting 44, 313–350.
Siegel, H.O., Winkler, H.A., Boniwell, J.B., 1957. Discovery of the Mobrun Copper Ltd. sulphide deposit, Noranda Mining District, Quebec. In: Methods and Case Histories in Mining Geophysics. Commonwealth Mining Met. Congr., 6th, Vancouver, 1957, pp. 237–245.
Tarantola, A., 2005. Inverse Problem Theory and Methods for Model Parameter Estimation, first ed. SIAM, Paris.
Thompson, D.T., 1982. EULDPH – a new technique for making computer-assisted depth estimates from magnetic data. Geophysics 47, 31–37.
Tlas, M., Asfahani, J., Karmeh, H., 2005. A versatile nonlinear inversion to interpret gravity anomaly caused by a simple geometrical structure. Pure and Applied Geophysics 162, 2557–2571.